Performance Assessment of Cerenkov Emission Imaging

Emma Mellhammar

Supervision

Johan Axelsson and Sven-Erik Strand

This work has been conducted at
Department of Physics and
Department of Medical Radiation Physics,
Lund University.

Abstract

Background: Cerenkov Luminescence Imaging detects the light emitted when a charged particle travels through a medium with a velocity greater than the phase velocity of light in that medium. The beta-particles emitted from many radionuclides used in nuclear medicine have sufficient kinetic energy to satisfy the requirement.

Purpose: This thesis aimed to examine the physical and optical properties affecting the radiance of Cerenkov radiation measured in the new imaging modality Cerenkov Luminescence Imaging (CLI). In difference to established preclinical imaging modalities detecting radionuclides such as Positron Emission Tomography (PET) and Single Photon Emission Computed Tomography (SPECT), CLI detects Cerenkov emission. This radiation is within the optical spectral range, as opposed to high energy photons emitted as a product of the radioactive decay. Better understanding of these properties could possibly enable quantitative measurements of radionuclide uptake in animal tumor models.

Materials and method: Mouse-sized phantoms of varying scattering and absorbing properties with channels drilled at different depths were filled with ^{18}F and imaged with a laboratory-built CLI-system. Images of varying exposure times were collected repeatedly during a number of half-lives of ^{18}F. The radiance and FWHM were analyzed with MATLAB and the custom-made MATLAB-program OptiScope. For comparison to established imaging modalities, the phantoms were imaged in three different preclinical PET-systems, including the box-geometry system Genisys4 (Sofie BioSciences).

Results: The radiance of the Cerenkov radiation was found to be proportional to the activity present in the channels of the phantoms. Increasing depth of the cannels was found to decrease the radiance measured, as did increasing absorption coefficient. An increasing scattering coefficient was found to increase the radiance over the range examined. Increasing depth and scattering coefficient showed a broadening of the FWHM, while an increasing absorption coefficient narrowed the FWHM. The FWHM measured for a variety of depths down to 1 cm and varying scattering and absorption coefficients, ranged between 0.4- 3.8 cm.

Conclusion: CLI is limited by its complicated relationship between activity and radiance. Due to the many factors affecting the emitted light at the surface of the phantoms, the radiance could not directly be used as a quantitative measurement of the activity uptake. For this to be possible some form of normalization for the effective attenuation coefficient would be needed and the imaging could only be done for uptakes close to the surface of the subject. The coefficient could be assessed with an external light source.

CLI will never challenge PET as an equally efficient quantitative imaging modality for preclinical imaging, but could become a part of an imaging scheme where a combination of modalities is used to utilize the benefits of each system.

Populärvetenskaplig sammanfattning

Laddade partiklar med hög energi kan ibland färdas snabbare än ljusets hastighet i det medium det för stunden befinner sig i. När detta sker, emitteras så kallat Cerenkovljus. Ljuset ligger inom det synliga spektret och kan alltså detekteras med vanlig kamerateknik.

Många av de radionuklider som används för nukleärmedicinska undersökningar och terapier emitterar högenergetiska laddade partiklar när de sönderfaller. Dessa kan få tillräckligt hög hastighet för att vid passage genom kroppen emittera Cerenkovljus.

Nukleärmedicinska radionuklider används även för prekliniska metoder och tidigare studier har visat att Cerenkov Luminance Imaging (CLI), en metod där man studerar det emitterade Cerenkov ljuset från försöksdjur injicerade med radionuklider, skulle kunna användas för prekliniska studier av nukleärmedicinska terapier och läkemedel.

När ljus färdas genom vävnad kommer det spridas och absorberas och endast en liten del av ljuset, om något, kommer ta sig upp till ytan. Om man ska kunna kvantifiera vilken mängd radioaktivitet som gett upphov till ljuset, måste man ta reda på hur ljuset har påverkats av sin färd mot ytan.

I detta arbete utfördes så kallade fantommätningar för att studera hur spridning, absorption och djup i vävnad påverkar vilken mängd ljus man kan detektera. Fantomen bestod av mus-stora epoxiharts-block med olika optiska egenskaper som fick dem att absorbera och sprida ljuset olika mycket. Genom fantomen hade kanaler borrats med varierande avstånd till ytan för att simulera aktivitetsupptag på olika djup i en muskropp. Försöken gjordes med en ljustät låda som stänger ute vanligt ljus och en så kallad CCD-kamera monterad inuti lådan som kan detektera ljuset. Fantomen fylldes med radionukliden ^{18}F, en vanlig nuklid vid PET-undersökningar och placerades i CLI-lådan. Bilder med varierande insamlingstid togs upprepade gånger under flera timmars tid, medan aktivitetsinnehållet i fantomen sönderföll.

För att jämföra CLI:s potential som nukleärmedicinsk bildverktyg utfördes Positronemissionstomografi (PET)-undersökningar av samma fantom med ^{18}F i tre olika prekliniska PET-system, däribland det box-geometriska systemet Genisys4.

Resultaten visade att radiansen sjönk som funktion av djupet och för stigande absorptionsegenskaper i fantomens material. Spridande partiklar i fantomen ökade radiansen. Upplösningen blev sämre för ökande djup och för stigande mängd spridande partiklar. Absorberande material förbättrade upplösningen något.

Resultaten visade på de hinder som måste överbryggas för att CLI ska kunna användas som ett kvantitativt nukleärmedicinskt bildverktyg, eftersom ljuset som detekteras inte direkt kan översättas till ett radionuklidupptag i muskroppen. Först måste radiansen normeras mot en effektiv attenueringskoefficient som beskriver hur ljusets intensitet förändras på sin väg mot ytan. Dessutom kommer CLI bara kunna användas till ytligt belägna aktivitetsupptag, så som tumörer implanterade under huden på försöksdjur.

Contents

Introduction

In recent decades preclinical imaging systems such as Single Photon Emission Computed Tomography (SPECT), Positron Emission Tomography (PET), Computed Tomography (CT) and Magnetic Resonance Imaging (MRI) have become leading techniques for monitoring biological and molecular processes [1]. These systems give opportunities to study molecular and metabolic transport pathways as well as giving insight into tissue functionality and pathology. The introduction of these modalities for small animal imaging has opened up new opportunities to assess new imaging markers and drugs, as well new techniques to study the diseases themselves. In some cases, these developments can be directly converted to clinical applications, while other form advances in preclinical imaging itself.

PET is becoming an important tool for studies of cellular and molecular processes [1]. It can be used for quantitative studies of biological and molecular processes in vivo, through labeling compounds with positron emitters. PET radionuclides, such as ^{11}C and ^{18}F, have the advantage of forming radiotracer compounds which do not change the biological behavior of the tracer, compared to many radionuclides used for SPECT. But, they often have quite short half-lives, which puts a restraint on their availability and are therefore more demanding to work with [2].

PET and the other imaging modalities differ slightly in function and abilities, but seem to have one crucial property in common: they are all quite expensive. The machines are costly to buy and run, and large studies with many experimental animals will demand ample machine time, increasing the cost even more. Only larger institutions will afford to invest in the necessary equipment, and research teams will have to wait in line to perform their studies.

There is therefore a demand and interest to create simpler and cheaper imaging techniques, that can be utilized in smaller laboratories in connection to other equipment necessary when working with laboratory animals.

With a simpler PET model, the Genisys4 TableTop PET (Sofia Biosciences, Culver City, CA) takes care of some of the extra weight put on by preclinical PET systems, by reducing the number of crystals to four detector panels, arranged in a box geometry. The system is smaller than most preclinical PET-systems and fit on a desktop, preferably next to the computer workstation.

The relatively new imaging modality Cerenkov Luminescence Imaging (CLI) has raised hope of a new tool for bio-imaging. It makes use of the Cerenkov radiation emitted when a charged particle with sufficient energy passes through a dielectric medium, e.g. a positron emitted from a PET radiotracer.

The challenge for CLI is to quantify the light signal as a function of the activity of the radiotracer. Since the emitted Cerenkov light is a function of many parameters, this is more easily said than done. Pioneering research groups have taken the initial and vital steps to prove the possibility to use CLI for quantitative preclinical bio-imaging studies. But for it to truly challenge the established imaging modalities a sure connection between radiance and radioactivity, taking into account the effect of tissue absorption, scattering and depth, must be set up. Also, the systems sensitivity and spatial resolution must be examined and described.

The work presented in this thesis aimed to investigate the physical and optical properties affecting the radiance measured in CLI measurements. Phantoms with varying scattering and absorption properties as well as varying depths for the positron emitting radionuclide were constructed. Using

this approach, the effect of the properties on radiance and spatial resolution could be studied one at a time. This gave an opportunity to evaluate the obstacles in need to be bridged if CLI is ever to be used for quantitative studies. To give a perspective of CLIs performance the same phantoms were imaged in three different preclinical PET-systems, including the Genisys4.

Basic theory

Cerenkov radiation

When a high speed charged particle travels through a dielectric[1] medium, its associated electromagnetic field will polarize the medium along its path. Electrons of the atoms in the medium become displaced, creating the local polarization. This is not a form of excitation and neither is the electron removed from its bound state, but a displacement of the electron in the medium´s lattice. When the electrons return to their normal positions they radiate photons. In the normal case, these will interfere destructively with each other and is therefore never seen. But, if the velocity of the charged particle is greater than the phase velocity[2] of light in the dielectric medium, the emitted waves (wavelets) from each polarized point in the medium will interfere constructively since all the points are in phase. Coherent radiation is then emitted [3].

The proof for the origin of Cerenkov radiation was originally given by Pavel Alekseyevich Cerenkov, who won the Nobel Prize for his discovery in 1958 together with Ilya Frank and Igor Tamm.

For a charged particle travelling from point A to B (see Figure 1 below) in a dielectric medium with the refractive index n at the velocity v_p, coherent Cerenkov radiation will be emitted while $\frac{c}{n} < v_p < c$, where c is the speed of light in vacuum. The ratio between the velocity of the particle and the speed of light in vacuum is often denoted $\beta = \frac{v_p}{c}$. The wave front lies along the line AC and the emitted waves travel with the velocity $v_m = \frac{c}{n}$. For a time interval Δt the particle will travel the distance $AB = v_p \Delta t = \beta c \Delta t$ and the emitted waves will travel the distance $AC = v_m \Delta t = \frac{c}{n}\Delta t$.

This gives the Cerenkov relation, namely

$$\cos\theta = \frac{AC}{AB} = \frac{1}{n\beta}$$

Equation 1

---

[1] A dielectric is an electrical insulator, meaning it can be polarized by an applied electric field. When having an external field applied, charges do not flow through the medium as with a conductor, but are only slightly displaced from their average position, causing a dielectric polarization.

[2] Phase velocity is the rate at which the phase of a wave propagates. This is not the same as group velocity, which is the velocity with which the envelope of a wave propagates. The phase velocity does not carry any energy or information, which is why there is no limit for particles to have a greater velocity than the phase velocity.
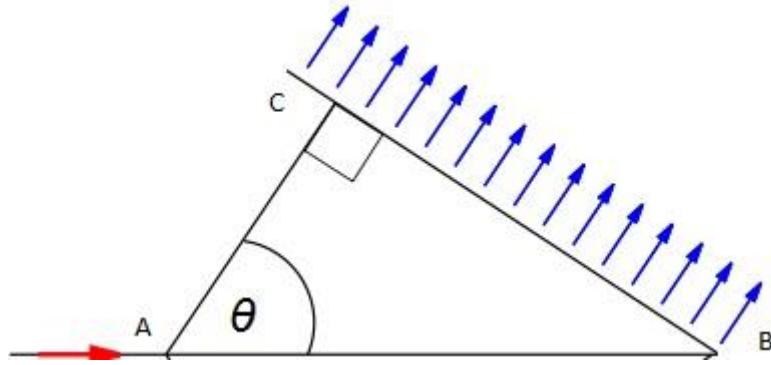
Figure 1 The charged particle traveling from point A to B with a velocity greater than the phase velocity will emit Cerenkov radiation along the line BC at an angle θ to the particle.

The quantity β is related to the kinetic energy E of the particle and its rest mass m. When the particles velocity is close to the speed of light, its energy can be calculated trough the relativistic relationship

$$E = mc^2 \left[\frac{1}{\sqrt{1 - \frac{v^2}{c^2}}} - 1 \right] = mc^2 \left[\frac{1}{\sqrt{1 - \beta^2}} - 1 \right]$$

Equation 2

Equation 2 can be used to calculate what kinetic energy for a charged particle of mass m equals a velocity which satisfies the condition $v_p > \frac{n}{c}$, where n is the refractive index of the medium through which the particle is traveling.

From Equation 1 two important conditions can be observed. The equation has a threshold when $\beta = \frac{1}{n}$ and $\theta = 0$ and there is a maximum angle θ at which Cerenkov radiation can be emitted. When $\beta \rightarrow 1$ i.e. when the particle velocity grows closer to the velocity of light in vacuum, c, the maximum angle is given by

$$\theta_{max} = \cos^{-1} \frac{1}{n}$$

Equation 3

We can also observe that as the refractive index increases, the threshold velocity for Cerenkov radiation from the particle decreases. A charged particle will therefore need a lower velocity to emit Cerenkov radiation in water than in air, since air has a lower refractive index than water.

The Frank-Tamm equation

As mentioned earlier Cerenkov shared his Nobel Prize with two other scientists. They gave the theoretical description of the Cerenkov radiations origin. The amount of Cerenkov radiation emitted for a given frequency can be calculated by the *Frank-Tamm formula* [3]. The energy dE emitted per path length dx traveled by the particle per angular frequency dω can be calculated as

$$dE = \frac{\mu(\omega)q^2}{4\pi}\omega(1 - \frac{c^2}{v^2 n^2(\omega)})dx d\omega$$

<div align="center">Equation 4</div>

Here $\mu(\omega)$ is the frequency dependent permeability of the medium and q is the charge of the particle. By integrating Equation 4 over the angular frequency, the total energy radiated per unit length is given by

$$\frac{dE}{dx} = \frac{q^2}{4\pi}\int_{v>c/n(\omega)} \mu(\omega)\omega(1 - \frac{c^2}{v^2 n^2(\omega)})d\omega$$

<div align="center">Equation 5</div>

The Frank-Tamm formula gives the relationship

$$\frac{dE}{d\omega} \propto \omega \rightarrow \frac{dE}{d\lambda} \propto \frac{1}{\lambda^3}$$

<div align="center">Equation 6</div>

This tells us that the emission is inversely proportional to the cube of the wavelength, an explanation to why the Cerenkov radiation is most intensive for shorter wavelengths and appears blue [3].

As shown by several, the Frank-Tamm formula can be integrated for a given interval of wavelengths [4, 5]. The formula calculates the number of photons in a given region of wavelengths produced along the particles path.

$$\frac{dN}{dx} = 2\pi\alpha \left(1 - \frac{1}{\beta^2 n^2}\right)\int_{\lambda_1}^{\lambda_2} \frac{1}{\lambda^2} d\lambda$$

<div align="center">Equation 7</div>

This equation shows that the spectral distribution of the Cerenkov intensity is inversely proportional to the cube of the wavelength, leading to the peak of the photon spectrum in the visual range of light to be at the shorter wavelength, namely the blue.

From Equation 5 we can see that the spectrum of the Cerenkov radiation is continuous. The upper limit of the spectrum (i.e. shorter wavelengths) is when n becomes less then unity, i.e. when Equation 1 is not satisfied. This happens when the emitted radiation gets up to about X-ray frequencies. The refractive index is a function of frequency (and therefore also wavelength, this is called dispersion), as the frequency is increased the refractive index decreases, and as it becomes less than unity the condition is no longer satisfied. The lower limit (for longer wavelengths) occurs because of self-absorption in the medium [3].

Continuous slowing down approximation

A charged particle travelling through a medium will collide and scatter against atomic electrons and nuclei through elastic and inelastic collisions. This will reduce the energy of the particle and change

its direction. A common definition of the range of the charged particle is calculated with the *Continuous slowing down approximation* (CSDA):

$$R_{CSDA} = \int\limits_0^{E_0} \left(\frac{\mathrm{d}x}{\mathrm{d}E}\right) dE = \int\limits_0^{E_0} \left(\frac{\mathrm{d}E}{\mathrm{d}x}\right)^{-1} dE$$

Equation 8

This is the range travelled by the charged particle after losing all its initial energy E_0. To find the range the particle travels while emitting Cerenkov radiation, the lower limit of the integral in Equation 8 can be set to the limit energy calculated from Equation 2.

The quota $\frac{\mathrm{d}E}{\mathrm{d}x}$ is often called the stopping power and is meant to cover all forms of energy losses a charged particle experiences along its path, why it sometimes is given the subscript $\left(\frac{\mathrm{d}E}{\mathrm{d}x}\right)_{tot}$.

Optics in biological tissue

With discussing light in optical imaging one refers to electromagnetic radiation with wavelengths between a few hundred up to about a thousand nanometers. It includes the visible range, which ranges from about 400 to 700 nm, ultraviolet radiation and also the near and far infrared region of the electromagnetic spectrum. In imaging the wavelengths above 650 nm are of special interest as this is called the water window, or the diagnostic window. It has minimal attenuation of light due to absorbers and has still a low level of absorption due to water [6].

Biological tissues can be broken down into the cells, their organelles and the intra- and the extracellular structures. Within the complex matrix there is a constant variation of refractive indices between the different structures and many different absorbing chromophores.

Radiance

Radiance (L) is a measure of the quantity of radiation passing through a surface within a given solid angle. The SI unit of radiance is one watt per steradian per square meter (1 W sr^{-1} m^{-2}). But, in optical imaging radiance is often given as the number of photons passing through a surface for a given solid angle per second (1 p s^{-1} cm^{-2} sr$^{-1)}$. This is the reason why in the literature, the relationship between the intensity of the emitted Cerenkov radiation and its wavelength is so often described as $1/\lambda^2$, instead of $1/\lambda^3$ as given by the theoretical description by Frank-Tamm in Equation 6. In both cases however, the peak of the intensity of the Cerenkov radiation will be at shorter wavelengths, i.e. blue light. Unlike fluorescence, the Cerenkov radiation spectra is continuous, without characteristic spectral peaks [7].

Scattering

Light scattering is the redirection of the path of photons [8]. Scattering of light in biological tissue is believed to be because of the varying refractive indices between structures in- and outside of the cells. It causes the reflection, refraction and diffraction of light as it travels through the tissue. The average distance a photon travels in biological tissue before being scattered is in the order of 0.01-0.1 mm [6]. A light source embedded in tissue will therefore have a broader distribution at the surface. Also, structure size will affect the scattering within the tissue.

In a macroscopic approach to describe scattering in tissue, two quantities are used [9]. μ_s is called the scattering coefficient and gives the probability for scatter per unit length. The anisotropy factor is given by $g = \langle \cos(\theta) \rangle$ and gives the average scatter direction. In an isotropic medium where the probability for scattering is equal in all directions g=0. In tissue g=0.9, which equals scattering in a forward direction [6]. g=1 is when the scatter angle is zero and all light propagates in the forward direction.
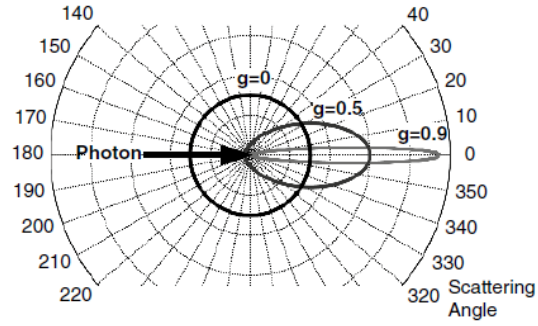
Figure 2 The anisotropy factor (g) describes the direction in which light is scattered. For an isotropic medium where the probability for scatter is equal in all angles _g_=0. As the probability approaches unity for the forward direction, the anisotropy factor approaches 1. Image from [6].

The reduced scattering coefficient μ'_s takes the anisotropy into account and is given by

$$\mu'_s = (1 - g)\mu_s$$

Equation 9

The wavelength dependence of the reduced scattering coefficient can be described as

$$\mu'_s = a\lambda^{-b}$$

Equation 10

Here _a_ is the scatter amplitude for the wavelength λ, it describes the density of spherical particles in the tissue, while _b_ is the scatter power and is a measure of the size of the sphere. The scatter power decreases when particle size increases [9]. The reduced scattering coefficient decreases as a function of wavelength but can be seen as constant over the optical window [6]. Absorption is much more wavelength dependent. For the study of Cerenkov light propagating through tissue from a point of emission, as in CLI, scattering will set a limit to the spatial resolution of the system.

Absorption

Absorption is the transfer of the photon energy to a molecule, resulting in the loss of energy [8]. It leads to an attenuation of light and a reduction of the light intensity. Absorption of light may happen when a photon with energy equal to the energy difference between two electron states in a chromophore, is incident on such a chromophore and excites the electron [9]. Absorption contrast can be utilized as a medical application, since there is a large difference between the absorption spectra of oxygenized and deoxygenated hemoglobin. The radiance of light transmitted through a tissue can therefore give a measure of the oxygenation level of blood in that tissue [6].

If scattering in tissue can be considered negligible, then the reduction of intensity for light traveling through tissue can be described by the _Beer-Lambert law_:

$$I_T(\lambda) = I_0(\lambda) \cdot e^{-\mu_a d}$$

Equation 11

In Equation 11 μ_a is the absorption coefficient and d is the distance travelled by the photon in the tissue. The absorption coefficient, as in analogy with the scattering coefficient, describes the probability of absorption per unit length. Intuitively, the probability for absorption of light at a given wavelength λ will be greater in tissues with high concentration of chromophores. The absorption coefficient can therefore be described as

$$\mu_a(\lambda) = \sum_i \varepsilon_i(\lambda)[C_i]$$

Equation 12

Here ε_i is the extinction coefficient, describing the probability for absorption of a photon of a given wavelength for the i:th chromophore and C is the concentration of the i:th form of chromophore. In Figure 3 below, the absorption coefficients of water and hemoglobin is plotted as a function of wavelength over the optical window. It shows an increasing difference between the two as the wavelength is decreased, closing in on the blue light of Cerenkov radiation. Blood is an important chromophore, and variation of blood content in different tissues can lead to a big difference in light absorption.
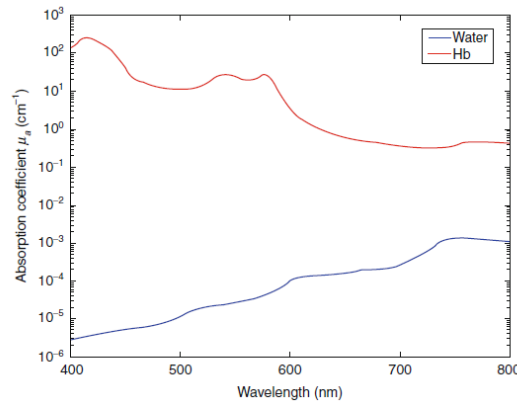

Figure 3 Absorption coefficient for water and hemoglobin as a function of wavelength. Image from [8].

For the study of Cerenkov light propagating through tissue from a point of emission, as in CLI, absorption will set a limit to the sensitivity of the system.

Effective Attenuation coefficient

To simplify the description of light deflection in tissue [9, 10], a combined coefficient for both scattering and absorption can be described as

$$\mu_{eff} = \sqrt{3 \cdot \mu_a(\mu_a + \mu_s')}$$

Equation 13

The radiance at a surface from a source emitting light a distance R below the surface is then proportional to

$$L \propto \frac{e^{-\mu_{eff} \cdot R}}{R}$$

Equation 14

13

Absorbing chromophores

For the optical window in biological tissues, the most important absorbing chomophores are hemoglobin, water and lipids. Hemoglobin, the molecule transporting oxygen by the blood to all vital tissues in the body, can either be oxygenated or deoxygenated, giving it different absorbing properties. Water mainly absorbs in the near infrared region of wavelengths. Lipids are similar to water in mostly absorbing at longer wavelengths. As described in Equation 12, the absorption coefficient can be described as the sum of the concentration times the extinction coefficient for each chromophore. Considering the most important chromophores, μ_a becomes

$$\mu_a = \varepsilon_{Hb}C_{Hb} + \varepsilon_{HbO_2}C_{HbO_2} + \varepsilon_W C_W + \varepsilon_L C_L$$

Equation 15

Here ε_{Hb}, ε_{HbO_2}, ε_W and ε_L are the extinction coefficients for deoxygenated hemoglobin, oxygenated hemoglobin, water and lipids. C_{Hb}, C_{HbO_2}, C_W and C_L are the concentrations of deoxygenated hemoglobin, oxygenated hemoglobin, water and lipids.

Cerenkov Luminescence Imaging

As described previously, Cerenkov radiation has been long known, and observed in other areas. But it was only recently the idea of using it for optical imaging of radiotracers was presented. Originally the emission of Cerenkov radiation from ^{18}F, a common radiotracers used both clinically and pre-clinically, was shown by Cho et al [11]. They used a CCD to detect light emitted from a microfluidic chip filled with [18]F. By assessment of the light properties, they showed that Cerenkov radiation was the likely source of the light.

CLI systems

In a large part of the articles published on CLI, the studies have been done on equipment built for preclinical in vivo optical imaging, such as bioluminescence. An often quoted system is the Xenogen IVIS 100 or 200 (Caliper Life Sciences) [5, 12, 13].

The Charged Coupled Device

Charged coupled device (CCD) is the most common detector used for various optical imaging modalities. The inventors of the CCD were honored with the Nobel Prize in Physics 2009. CCDs are made up as a grid of elements similar to capacitors, acting as potential wells for electrons [6]. Incident photons create free electrons through photoelectric effect. These electrons are then trapped in a well and remains there with a linear relation between the number of incident photons and the created number of electrons. But the linearity can be disrupted. When a well is almost full it can be difficult for new electrons to enter the well. The trapped electrons create a negative electric field which can limit new electrons from entering a well or may lead to electrons spilling over into neighboring wells. The wells are emptied when an external electrical field is applied. This makes all the electrons move simultaneously, why the information about the incident photons per element/well is preserved. One row or column in the grid is emptied at a time by being shifted with an electrical field onto an analog-to-digital converter (ADC).

The sensitivity, or more precisely the quantum efficiency, of a CCD is in the range of 95% in dedicated wavelength regions [6]. This means that a photon has a 95 % chance to add electrons to the pixel well. The sensitivity will be affected by read out noise, i.e. electrons added or lost from the signal during the amplification. Dark noise arises mostly from electrons released from thermal energy. Cooling the CCD lowers the dark noise, but this is only helpful when the system is used for long exposure times.

Early work in CLI

The idea of CLI was first proposed by Robertson et al. They showed that two different radiotracers labeled with high energy positron emitters, ^{18}F and ^{13}N, emit Cerenkov radiation after decay in a medium and can be detected with a CCD [12]. They gave proof-of-concept for using radiotracers in *in vivo* studies of the emitted Cerenkov radiation. Robertson et al, imaged well-plates prepared with various activities of positron emitting radionuclides, showing that the signal increased linearly with increased activity. They also showed that the radiance from ^{13}N for a given activity was higher than from [18]F. This was explained with the higher average energy of the emitted positron from [13]N. A subsequent experiment was performed in which the activity was mixed with solutions of varying refractive index. The study showed that the radiance increased as the refractive index increased. This was explained consistent with the reduction of the speed of light, and therefore reduction of the

threshold energy required for the charged particle to produce Cerenkov radiation, when the refractive index increases.

Shortly after Robertson et al. published the first article on CLI, Liu et al. showed that light was emitted from ^{18}FDG, Na^{18}F, Na ^{131}I, ^{90}YCl$_3$ and a ^{90}Y labeled tumor targeting peptide, and that the probes could be imaged in vivo with optical imaging [14]. They also ruled out that the CCD signal of these probes was contributed by either β^+ or β^- by covering the sources with black and white paper, which resulted in a loss in signal, with the black paper showing a better signal blocking. Optical photons would be expected to be stopped by paper, while high energy β-particles could penetrate the barrier. They also concluded that the likelihood of the origin being Cerenkov radiation was strengthened by the continuity of the detected spectrum and the increased light output as the refractive index of the medium increased.

Ruggiero et al. added more radionuclides to the list of possible probes for CLI. They evaluated the positron emitters ^{18}F, ^{64}Cu, ^{89}Zr and ^{124}I, the β-emitter ^{131}I, and α-particle emitter ^{225}Ac [15]. Solutions of decreasing activity concentration in water were imaged with optical imaging. The positron emitters were also imaged with PET. For all the radionuclides, a linear correlation between the radiance and the activity concentration were found. The radiance was plotted against time. A linear regression analysis between the reduction of radiance against the radioactive decay gave a good correlation (R=0.98), indicating that the light detected originated from the decay of the radionuclide. As a quantitative assessment of the images, the average radiance versus the mean activity measured by the PET on the positron emitting radionuclides were plotted, showing a linear relationship. It was taken to suggest that CLI could be used for quantitative studies. Similar experiments had previously been performed by others [12, 14].

With the help of Equation 2, the threshold energy for a charged particle passing through a medium of refractive index n to emit Cerenkov radiation can be calculated. For water, which has a refractive index of n=1.33, the particle must have a velocity of 0.75c or higher to produce Cerenkov radiation. From Equation 2 this gives a threshold energy for a positron of 264 keV. ^{225}Ac is a pure α-particle emitter, emitting α-particles with an energy range of 5.021 to 5.830 keV, a considerably higher energy than the most energetic positrons studied by Ruggiero [15]. But due to the α-particles much larger mass, the velocity of the particles are below the threshold for Cerenkov radiation. To explain the light detected from ^{225}Ac it has been suggested that it is produced by emissions form daughter nuclides, among which there are many β-emitters whose particles have a sufficient energy to produce Cerenkov radiation [16].

Cerenkov radiation from radiotracers has opened a window for other forms of optical bio-imaging techniques. Most optical techniques, e.g. fluorescence imaging, are restricted to preclinical use since only a very few fluorescent substrates are approved for clinical use [17]. Radiotracers, on the other hand, are a much larger family of substrates approved for clinical use, which encourages the hope that CLI might have some clinical applications in the future.

It has been stated that CLI, as a potential advantage over PET in preclinical studies, could speed up the process of small animal imaging. Instead of only having a single animal scanned as in a PET system, in a CLI system up to five animals could be simultaneously scanned, with a complementary white light image for anatomical reference [17].

16

Assessment measurements in previous studies

In the pivotal article on CLI, by Robertson et al., they discussed the limitations of CLIs in vivo imaging applications. They stated that absorption and scattering of the Cerenkov light would lead to low light output and a blurring effect [12]. But in advantage to PET, they also considered the fact that production of Cerenkov light precedes the annihilation of the positron, making the origin of the Cerenkov radiation closer to the point of decay of the radionuclide.

In their primary article on CLI, Liu et al. performed a phantom imaging study to evaluate the spatial resolution of ^{18}F, ^{131}I and [90]Y. They found that for all of them, a spatial resolution of 1.2 mm could be achieved [14]. Robertson et al. argued in their following study on CLI in a pharmaceutical study that CLI analysis should include a normalization of signal by the injected dose [18].

Spinelli et al. did the first attempts at measuring the depth in vivo of the Cerenkov light source [4]. A mouse injected with [18]FDG was imaged with CLI technique and showed uptake primarily in the heart and the bladder. Two different methods for depth calculation were examined. The first one depended on the wavelength dependence for tissue scattering. By assuming a point source and a homogenous flat slab of tissue and using a multispectral assessment of the emitted light, assuming a standard diffusion approximation of the light propagating through the tissue, they calculated the depth to the heart of the mouse to be 1 mm. With a second method they took advantage of the spectral distribution of the Cerenkov radiation. Using the proportion between number of photons and wavelength being $1/\lambda^2$, the ratio of the integrated radiance of two different wavelengths can be calculated as

$$\frac{I_s(\lambda_1)}{I_s(\lambda_2)} = \frac{\lambda_2^2}{\lambda_1^2} \; e^{\mu_{eff}(\lambda_2) - \mu_{eff}(\lambda_1)d}$$

<div align="center">Equation 16</div>

From that the distance to the source *d* can be calculated as

$$d = \frac{ln\frac{I(\lambda_1)\lambda_1^2}{I(\lambda_2)\lambda_2^2}}{\mu_{eff}(\lambda_2) - \mu_{eff}(\lambda_1)}$$

<div align="center">Equation 17</div>

With the second method a depth of 1.6 mm where found. The result of the two methods was compared with the depth measured with MRI, found to be 1.5 mm. Boschi et al. used the two methods in attempt to measure the depth of a tumor in mice [19]. Only the second method could in this case be considered to estimate a reasonable depth of the tumor.

In the study by Park et al. about triple modality probes (described later), Sprague-Dawley rats were injected in the back muscle at depth 4 and 7 mm with different activity concentrations of [124]I [20]. At 4 mm and with an integration time of 1 min, the lowest activity concentration that could be detected was 0.3 µCi/µL. With a scan time of 10 min the lowest activity concentration detected for the same depth was 0.1 µCi/µL. At a depth of 7 mm, a 1 min scan time could detect a minimum activity concentration of 1 µCi/µL.

In vivo studies

Robertson et al. did in their initial article on CLI a test where they detected the light emitted from a mouse carrying a human prostate tumor injected with [18]FDG [12]. This was followed by a study with two mice with a colon tumor on their flank. The animals were imaged with both PET and CLI. It was shown from the PET that one of the tumors held a higher activity concentration. A similar relationship of the same proportions was noted in the CLI, implying a possibility to use CLI for activity assessments in preclinical studies.

Liu at el. injected [18]FDG in mice with implanted C6-Fluc glioma and imaged them with the IVIS Spectrum system (Caliper Life Sciences, Hopkinton, MA) for CLI and with a small animal PET system. [18]FDG could be localized and retained in the tumors with CLI. High signals were also detected in the bladder and brain. It was noted that the heart was hardy visualized in the CLI assessment due to its deep position in the mice. The organs were removed from the body of the mice and imaged again. High activities were mainly observed in the heart and tumor. A quantitative analysis of the images from both CLI and small animal PET showed good correlation of activation uptake in the organs between the two imaging modalities [14].

When it had been shown by several studies that a correlation could be found between activities of a radionuclide measured with PET and the measured radiance from the same either phantom or mouse measured with CLI [12, 14, 15], Robertson et al. took the step to show how CLI could be used in a pharmaceutical drug study [18]. Mice inoculated subcutaneously with B-cell lymphomas where imaged with [18]FDG both in a PET-system and in CLI, giving baseline imaging of the signal from the tumors. The quantitative measurements of the tumor size and uptake were done with PET. The mice where divided in two groups, where one group was given MLN4924, an antitumor agent known to efficiently shrink lymphomas. The mice of both groups were imaged several times, following the uptake and size of the tumors. The PET-imaging showed a reduction in tumor growth and also shrinkage in the treated group and continued growth in the untreated group. The measured radiance and radiance per injected dose showed a correlation with the development measured with the PET system.

Holland et al. showed in a study the potential of using CLI "as a tool facilitating image-guided surgical identification and resection of tumors based on the optical signature of localized radiotracers" [21]. They used a CLI-system to image a mouse before, during and after surgical resection of HER2/neu positive xenografts. The mouse had beforehand been administrated [89]Zr-DFO-trastuzumab, a radiotracer with a known high specific uptake in the mentioned tumor. The average radiance from the tumor was before the surgical incision about $1 \cdot 10^4 \, \mathrm{p \, s^{-1} \, cm^{-2} \, sr^{-1}}$. After the mice was opened and the tumor was freely exposed the radiance increased to an average of $1.4 \cdot 10^4 \, \mathrm{p \, s^{-1} \, cm^{-2} \, sr^{-1}}$, due to less attenuation and scattering in the skin that was now removed. After they had removed the tumor, they imaged the mouse again and showed a complete loss of signal from the site where the tumor recently sat. After the mouse was closed a last image was made, showing no optical signal. They also made a note of the fact that the absolute amount of [89]Zr activity in the tumor post resection was only 20.4 kBq, which they considered a low concentration but apparently sufficient to give a guiding signal for the incision.

Clinical applications

In addition to the expectation of CLI becoming an important tool in preclinical molecular imaging, hopes have been raised that it could also contribute in clinical applications [17]. Due to the poor tissue penetration of Cerenkov radiation the development has been focused on clinical applications where radionuclides are used to be absorbed at shallow locations in the body. An interesting area is treatment of thyroid gland cancer with ^{131}I, together with other radioactive iodine isotopes also known as radioiodine. Its main decay mode is through β-decay, emitting negatively charged beta paticles, which has no simple method for detection.

Jeong et al. made the first study that demonstrated the potential of CLI using radioiodine for both in vitro and in vivo application for thyroid studies [22]. They measured light emission from ^{131}I and ^{124}I assays in well-plates with many different activity concentrations and found that both radioiodine isotopes had a linear correlation between dose and luminometric intensity.

Further, their study used anaplastic thyroid cancer cells and rat thyroid cells incubated with ^{124}I imaged in a well-plate geometry. They found an increased light intensity with increasing number of cells. The light intensity showed a positive correlation with the radioactivity of the cells. For in vivo studies, nude mice where implanted with anaplastic thyroid cancer cells in three different positions with different amounts of cells. The mice were then injected with either ^{124}I or ^{131}I. The imaging of the luminescence showed clear visualization of all three implanted tumors and the luminescence intensity increased with increasing number of cells. But, the PET imaging with ^{124}I carried out for comparison also showed uptake in the thyroid gland and in the stomach. The study also examined the uptake of ^{124}I and ^{131}I in naked mice (now without any implanted cancer or thyroid cells). The luminescence imaging detected emission from the neck of the mice after injection of ^{131}I and ^{124}I. Again, a correlation was found between the light emission and the measured activity from PET imaging of the same mice. Jeong et al. concluded that CLI can be used for radioiodine uptake in tumors for animal models. They discussed that for CLI to be used for in vivo thyroid study, new CLI techniques under development such as Cerenkov Luminescence Tomography, CLT, that in the future might compensate for the poor tissue penetration of Cerenkov radiation, would be needed to make it possible.

Spinelli et al. showed in a recent study that they could obtain a planar image of Cerenkov radiation from human tissue of a patient treated with 550 MBq of ^{131}I for hyperthyroidism [23]. They called this new imaging modality Cerenkography. Spinelli et al. used a cooled Electron multiplied charged coupled device (EMCCD), connected to a lens. The EMCCD was used in a light tight room. To avoid reflections from ambient light, the patents body was covered in black cloth. The EMCCD was placed 50 cm from the patients head and neck. For anatomical reference, a photographic image was taken before the Cerenkov image.
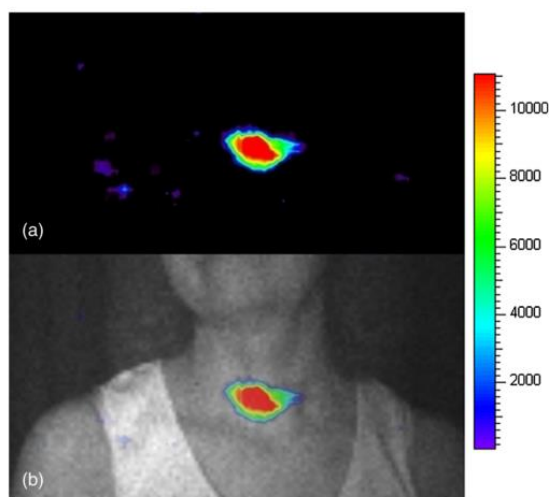
Figure 4 The first Cerenkography image taken by Spinelli et al.[23]

The image showed a good localization of the thyroid region.

Thorek et al. showed the potential to use Cerenkov radiation for lymphography [24]. They showed how lymph nodes in rats could be localized with injection of ^{18}F and removed by Cerenkov guided surgery. Dothager et al. suggested Cerenkov Radiation Energy Transfer (CRET) Imaging as a way to make use of the Cerenkov radiation from radioisotopes to create a stronger signal. They showed that Cerenkov radiation can be used to activate fluorescent nanoparticles to emit highly red-shifted light. This is a potential method to increase tissue penetration [7]. Kothapalli et al. demonstrated the possibility to use Cerenkov radiation for endoscopic imaging [25]. They used a fiber optic cable made for endoscopy connected to an optical imaging lens and a CCD. They showed detection of Cerenkov radiation both in non-invasive in vivo imaging of mice bearing C6 glioma and injected with ^{18}F and *ex vivo* imaging of organs from such mice.

Simulations

To quantify the radiance from a Cerenkov light source, we need methods to calculate what intensities we could expect. The Cerenkov light intensity depends on the activity of the radionuclide, the energy distribution of its emitted charged particle (i.e. the source for the Cerenkov radiation), the depth of the source and the optical properties of the tissue through which it penetrates. Simulations have been made to estimate what radiance can be expected at the surface due to a deeply embedded Cerenkov source.

A first attempt at quantifying the yield of photons from β-particle emitting radionuclides in water was done by Ross [26]. Ross explained that in order to determine the total photon yield from a Cerenkov event the Frank-Tamm equation (Equation 7) should be integrated over the particle path length, but this is not easily done, since the particle velocity is reduced as it propagates through the water making β a function of the particle energy, and the path length is in itself a function of the particles original energy. Also, the threshold energy for Cerenkov radiation has to be considered. Ross developed a calculation that integrated all these factors for the specific case of an electron in water up to electron energy of 4 MeV. The result presented the number of photons produced by an electron of a tabulated energy divided into spectral regions with a width of 50 nm from 250 nm to 600 nm. To get the full number of photons produced one can simply add the photons of the different spectral regions.

In their calculations, Mitchell et al. began with Equation 7 and considered its different factors [5]. By considering the energy distribution of the emitted β-particles from the radionuclides ^{18}F and ^{90}Y, they showed that about 47 % of the emitted β-particles from ^{18}F are above the threshold for Cerenkov radiation in water, while about 90 % of the β-particles from ^{90}Y are above the threshold. With the help of Equation 7, the expected number of photons emitted per unit length within the wavelength range can be calculated as a function of β-particle energy. For a given energy, the expected number of photons in water can be calculated, but it does not cover the whole spectrum. And, it has to be taken in to account that while traveling through the water, the β-particle will lose energy and slow down. That leads to a lower number of photons produced per unit length, and the total number of photons will be lower than predicted. Mitchell et al. performed Monte Carlo simulations in which the β-particle emission energy spectrums from the radionuclide of interest were modeled, as well as the change in Cerenkov radiation intensity [5]. They also included the possibility of Cerenkov radiation being produced by secondary electrons. A point source was assumed at the center of a volume of water. They found that for ^{18}F that the average number of photons per decay is 1.4 photons. The equivalent number for ^{90}Y was 57 photons per decay. If the refractive index was raised from 1.33 (water) to 1.4 (a refractive index similar to that of tissue) the number of photons per decay for ^{18}F was 2.4 and 69 for [90]Y. They compared their estimations to in vitro measurements, imaging well-plates with known activities of ^{18}F and ^{90}Y in water solutions. By measuring the number of emitted photons per second, and from the known activity calculate the emitted number of photons per decay, the result can be compared to the expected number of photons from the simulations. Due to the geometry of the CLI system and the camera efficiency, they expected to detect less than 50 % of the calculated number of photons, i.e. 0.73 photons per decay for ^{18}F and 28 for [90]Y. They detected 0.78 photons per decay for ^{18}F and 23.7 photons per decay for ^{90}Y, which was considered to be in good agreement with the estimation.

Beattie et al. performed a similar simulation, also using the Monte Carlo method, simulating the expected radiance from models of phantoms they then could make a practical measurement on [13]. In their calculations, they took into account the effect of secondary electrons produced by γ-rays and annihilation photons and estimated their contribution to the total number of Cerenkov photons. Their models gave the opportunity to vary both the refractive index of the tissue and the photon cross-section, which will affect in what size secondary electrons are produced. They found a good match between their expected number of photons per disintegration (decay) and the measured radiance from the experimental comparison for a number of radionuclides. This could also be shown for radionuclides decaying in tissues of a varying refractive index. They also ventured to model the intrinsic spatial resolution for a number of radionuclides, by modeling the point spread function.

Ackerman and Graves dug deeper into the potential of using CLI for imaging of α-emitting radionuclides by simulating the emitted Cerenkov radiation from a number of radionuclides [16]. It had been previously shown that Cerenkov radiation could be detected from the α-particle emitting isotope [225]Ac [15], but the production of the emission had not been thoroughly studied. As for all charged particles, the energy necessary to produce Cerenkov light is calculated from Equation 2. Since the α-particle is much heavier than electrons and positrons, this threshold is much higher, and the energy available from α-decay is normally not enough. The α-particle has enough energy to ionize the medium creating free electrons, but these are not of sufficient energy to produce Cerenkov light. But, many of the progenies of the α-particle emitters produce γ-rays of sufficient energy to create electrons with kinetic energies over the Cerenkov threshold. Also, the decay chains

may include β-emitters producing Cerenkov light when of sufficient energy. Obviously all this makes the assessment of α-particle emitting radionuclides for CLI slightly more complicated than β-emitting ones. Ackerman and Graves showed that the Cerenkov radiation from an α-particle emitting radionuclide won't be proportional to the activity until equilibrium is reached in the decay chain. For chains with long half-lives this factor disqualifies them from practical use in CLI. Also, if the Cerenkov light is not emitted from the first step in the decay chain, but produced by the emission of the radionuclides progeny, then the delay between the initial decay and the Cerenkov emission dissolves the relationship between the origin of the light and the position of the activity. Ackerman and Graves simulations showed that radionuclides that only decayed though α-particle emission produced few Cerenkov photons. The data showed that the Cerenkov radiation originated from γ-rays from nuclear de-excitations and Compton scattering producing electrons of sufficient energy. Ackerman and Graves also found that the radiance per activity concentration is a geometry dependent parameter. They simulated the radiance from activity concentrations of different size and shape and found that the same activity concentration produced different radiances.

CLT and other adaptations of CLI

In the field of optical imaging, Optical Tomography (OT) has been considered as a method for permitting quantification of light emission and a localization of its origin [8]. In OT, as with other tomographic modalities, the emission is studied from multiple views to determine the depth of the source of the emission. This way, the spatial resolution can be improved. But, the technique suffers from the fact that the detected light has undergone several scattering and absorption events on its way to the surface, strongly dependent on the tissue it traverses on its path. This diffusion can partly be compensated with propagation models, called the forward problem, which take into account the scattering and absorption properties of different tissues.

Li et al. suggested that CLI could be used for tomographic studies, proposing the new method Cerenkov Luminescence Tomography (CLT) [27]. They described this technique as a way to measure the distribution of radioactive tracers inside a small animal, reconstructed from the surface measurement of Cerenkov photons using an inverse algorithm. By placing the object to be studied underneath a CCD and placing mirrors on each side of the object, reflecting the sides of the object towards the CCD, three different angles are imaged.

Park et al. reported a basic method for creating a triple modality imaging probe for CLI/PET/MRI [20]. By conjugating a PET radionuclide with sufficient β-particle energy to create Cerenkov radiation in tissue, with a magnetic probe, imaging in all three modalities can be combined to benefit from their respective advantages. Park et al. combined [124]I with thermally cross-linked, super paramagnetic iron oxide nanoparticles (TCL-SPION).

Positron Emission Tomography

Positron Physics

Positron emission is a form of nuclear decay (beta decay) where the nucleus emits a positron and a neutrino. The positron, being the antiparticle of the electron, only has a short lifetime, where it travels a short distance, the length of which depends on its kinetic energy, before it annihilates with an electron in the medium through which it travels. When doing so, two photons, both of 511 keV, are emitted at opposite direction. The angular distribution is of 0.5° FWHM at 180° [28]. For just a short while, before the annihilation happen, the electron and positron form a particle called positronium, which has a decay time of 10^{-10} s [29].

To detect the annihilation events, two detectors measuring the coincidental event of two photons of the right energy, is the technique used in PET systems. The line between two coincidental events is called the line of response (LOR). The annihilation is assumed to have happened somewhere along the LOR.

Radionuclides

For use in clinical PET, there are several positron emitters that are suitable. The most commonly used is ^{18}F, used frequently in the [18]FDG compound. It has a half-life of 110 minutes, which is long enough for labelling and uptake of compounds with fairly fast accumulation. For slower compounds, such as monoclonal antibodies in solid tumors, more long lived radionuclides such as [124]I or [89]Zr are suitable [30]. Among the shorter lived radionuclides, ^{11}C, ^{13}N and [15]O can be mentioned. Half-life, decay mode and maximum positron energy for common PET radionuclides are given in Table 1 below.

Table 1 Common PET radionuclides. Data from [30].

Nuclide	Half-life	Decay mode (%)	$E_{\beta+,max}$ [keV]
[11]C	20.4 min	β+ (99.8) EC (0.2)	960
[13]N	9.96 min	β+ (100)	1,190
[15]O	2.03 min	β+ (99.9) EC (0.1)	1,720
[30]P	2.5 min	β+ (99.8) EC (0.2)	3,250
[18]F	109.6 min	β+ (97) EC (3)	635
[124]I	4.18 days	β+ (25) EC (75)	2,140
[68]Ga	68.3 min	β+ (90) EC (10)	1,900
[89]Zr	3.27 days	β+ (33) EC (77)	902

Photon interactions

The main form of interaction for the 511 keV photons in biological tissue is Compton scattering [29]. The detected signal is therefore attenuated by photons being redirected away from their original LOR. They can still be detected as coincidences by the PET system, but may add to the number of scattered events (see Events below).

Detector design

To detect the annihilation photons, scintillator materials are the most common detectors in PET systems. Scintillator materials have the property of emitting light when energy is deposited by charged particles or high energy photons passing through them. The light emitted is proportional to the energy deposited, which gives the detector system a chance to discriminate against photons detected that has previously been scattered on their way from the annihilation point to the detector. To attenuate the high energy annihilation photons, the scintillator has to be dense. They should have

a high probability for photoelectric interactions, in which the whole energy of the photon is absorbed. Inevitably, Compton scatter will still be the most common interaction and thickness of the detector will therefore be crucial for the detector to fully stop a large fraction of the incident annihilation photons.

The PET systems time resolution, which is crucial to determine which detected events are to be counted as coincidences, is to a large extent limited by the scintillator decay time. This is the time it takes for the light emitted after the energy deposit in the scintillator to be collected and later on transformed to an electrical signal. This is most often done by photomultiplier tubes (PMTs), although newer systems are utilizing semiconductor readout devices [28]. The scintillator light is guided to a PMT, often through a glass window and hits a photocathode, which in turn releases electrons. These are multiplied through the tube by hitting a number of dynodes, releasing more and more electrons. The current is then used as the detected signal from the PET system.

The arrangement of the detectors is an important factor affecting the spatial resolution of the PET system. A common design is the block detector design, in which smaller pieces is cut into the scintillation block, forming an array of smaller detector crystals in a grid [28]. The space in between the smaller crystals is filled with a reflective medium, separating the small elements and creating a path for scintillation light to travel to the PMTs. Normally, the block detector is then connected to a small number of PMTs, avoiding the need for every small element to be coupled to its own PMT [28]. To increase the localization from which small crystal light is detected by the PMTs, the crystals can be cut with varying depths into the scintillation block. Light signals from the different small crystals then get a specific distribution over the PMTs, giving them a fingerprint useful to determine which crystal incoming scintillation light originated in [29].

In a discrete individual design the scintillation crystals are separated by a refractive material. Each crystal then creates a path for the light to travel along, down to the photo detector. This is preferably combined with semiconductor readout devices, where each crystal is connected to an individual detector. This kind of detector design is more common in research and small animal PET systems [28].

In a Continuous gamma camera detector, a matrix of PMT is coupled to one large scintillator block. Light emitted from the scintillator can be seen by several PMTs and the position of the interaction is decided by weighting the signal from the involved PMTs [29].

The arrangement of the detectors can be done in a variation of ways. The most common way is in a ring geometry [28, 29]. If larger detectors are used, such as continuous gamma camera detectors, the detectors can be arranged in a polygonal geometry. For example, as a hexagonal could be made out of six detector panels. Cheaper systems sometimes have partial ring geometries with movable panels covering a fraction of the full circle. These systems allow a lower number of LOR and have to be rotated to detect enough data to be topographically reconstructed.

Positron range
Due to the fact that the positron travels a short distance between the point from which it is emitted to the point for the annihilation, there is a fundamental limit in the PET systems spatial resolution. The distance depends on the positrons kinetic energy, which for a positron from ^{18}F has a maximum energy of 0.650 MeV [29]. The range also depends on the surrounding medium. The positron travels

longer distances in tissues of low density, such as lung tissue, than in high density tissues, such as bone. The scale at which the positron range affects the final resolution depends on the PET systems spatial resolution.

Acollinearity

At the annihilation, energy and mass must be conserved, for which reason the photons are emitted at 180°. But sometimes kinetic energy remains that reduces the angle between the photons, on average $\pm 0.25°$ FWHM [28]. As a consequence, this means that the LOR doesn't pass through the annihilation point. Acolliniarity therefore reduces the spatial resolution. To what extent depends on the detector ring diameter, with lager diameters leading to larger errors. If a Gaussian distribution is assumed, the blurring effect can be estimated as:

$$\Delta_{ac} = 0.0022 \cdot D$$

<div align="center">Equation 18</div>

Here D is the diameter of the scanner [29]. Reducing the diameter lowers the effect of acollinearity, but at the same time increases the DOI errors (see Spatial Resolution below). In animal PET systems, the diameter is quite small, why acollinearity is not a big problem [29].

Events

PET differs from other nuclear imaging techniques by not relying on collimation of the incident radiation to know its origin. Since two annihilation photons are emitted, the detection of two simultaneous, or as it is called, coincidental photons equals the detection of one decay event, or rather one annihilation event. Therefore, it is important to allow detection of photons that are not passing the detector perpendicular to its surface, and to have good solid angle coverage.

The detectors of a PET system is during a regular examination hit by a large amount of photons detected as events, but only a smaller portion are registered as coincidences. Out of these, only an even smaller portion is true coincidences originating from an annihilation event. True coincidences are the desired detections, contributing to the detection of activity uptake [28, 29].

Random coincidences are detected when photons from two different events are detected coincidentally as if originating from the same event [28, 29]. For this to happen, they need to be detected within the coincidence timing window (see below). They add false information about the position of activity in the studied volume and therefore blur the resulting images. Random events can be reduced by narrowing the coincidence timing window, but that will at the same time reduce the PET-systems sensitivity.

Scatter coincidences appear when either one or both of the annihilation photons from an annihilation event are scattered in the surrounding medium and therefore are deflected from its original LOR [28, 29]. They result in a loss of contrast in the resulting image. The amount of scattered coincidences is a function of the PET systems energy resolution, its ability to distinguish between true events and scattered, which through the scatter events have lost part of its energy. A PET-system with good energy resolution can reject more scattered photons. Still, one should remember that scatter events originate from real annihilation events, but will lower the spatial resolution as they are not detected along their original LOR. Scattered events are difficult to make corrections for, as the

fraction can vary a lot and depend on several factors such as the size of the object being imaged and the geometry of the PET-system [29].

Sensitivity

The sensitivity of a PET system depends on several physical and technical factors. For simplicity, sensitivity can be divided in two major components, intrinsic and geometrical efficiency [28].

Intrinsic efficiency

The intrinsic sensitivity depends on the properties of the material the detector is made of. Its (effective) atomic number and density determine the linear attenuation coefficient, i.e. its ability to attenuate the annihilation photons and ultimately detect its energy. Therefore, the intrinsic efficiency is easy to estimate based on the detector material and its thickness. Increasing the thickness of the detector allows for a greater attenuation, but comes at the price of greater DOI errors (see below).

Geometrical efficiency

The geometric efficiency depends on the detector design. A high efficiency is reached if the circumferential detector ring is covered with detector area, i.e. if the detectors are packed closely enough to not leave any uncovered area. Any intermediate area lacking the ability to detect an intrinsic photon, such as spacing in between detector elements, lowers the efficiency.

The geometrical efficiency can be increased either by reducing the detector ring diameter or by increasing the field-of-view. Reduction of the diameter increases the solid angle, but will also reduce the spatial resolution by increasing DOI errors (further described below).

Coincidence Timing Window

To discriminate against unwanted events, such as scatter and random events, the PET-system uses a coincidence timing window. Coincidental events that fall within the timing will be recorded as true events. The width of the timing window will determine the level of random events recorded as true events, a thin window will reduce the random events contribution to the total of events.

Spatial Resolution

Spatial resolution is the measure of how close two lines can be resolved from each other. In PET (and many other imaging systems) the spatial resolution is measured as the FWHM of a line spread function. The spatial resolution is a function of detector size, positron range and photon acollinearity among other factors.

The National Electrical Manufactures Association (NEMA) guidelines measure the spatial resolution with a small point source of ^{18}F in different points of the field of view. The FWHM of the PSF is measured in the resulting images. The images should be reconstructed with filtered backprojection with rampfilter [31].

Depth of Interaction Error

The Depth of Interaction error (DOI error) arises from the uncertainty of the depth in the detector crystal at which the interaction takes place. For LOR:s away from the center field of view, the LOR:s and its photons fall in at an angle towards the detector surface normal. Therefore the uncertainty of interaction depth leads to a broadening of the events point spread function which is equal to a spatial blurring [28].

Preclinical PET

Small animal PET, or preclinical PET, is increasingly being used for studying cellular and molecular processes. In comparison with other molecular modalities, it provides a highly sensitive and quantitative measurement of biological processes in vivo [1]. Dynamic processes can be studied in real time and be followed over longer periods of time, to see changes in the same animal. Among biological and physiological processes PET can be used to study are perfusion, metabolism, protein expression and enzyme activity [8]. PET also presents an opportunity in pharmacological studies, where it can be used to perform fast in vivo screening of drugs by quantifying their bio-distribution [8].

Most preclinical PET-systems are constructed in similar ways to clinical systems, but on a smaller scale. To be efficient for studies of bio-distribution in mice, the resolution must be better than for clinical systems, which is in the vicinity of 1 mm. The detector elements are often of a few millimeters and due to the much smaller ring diameters, acollinearity is not as much of a problem as with clinical PET-systems [8]. Small crystals create an advantage for preclinical PET, since crystal size will set the lower limit for the achieved spatial resolution. But, the use of a high number of small crystals will demand a high number of electronic channels for the individual signal processing [2]. Crystal thickness affects the spatial resolution, especially at the edges of the FOV, due to DOI errors. But there are suggested DOI measurements that make use of the interaction depth to improve spatial resolution [2].

The sensitivity of the preclinical system is mainly affected by the solid angle coverage and the intrinsic efficiency of the detectors for the annihilation photons energy 511 keV [8]. To improve the SNR, acquisition time and injected activity can be increased, but this is limited by the count rate capability of the detector.

The reconstruction methods are basically the same as for clinical PET. Iterative algorithms such as Maximum Likelihood Expectation Maximization (MLEM) and Ordered Subset Expectation Maximization (OSEM) are used to create a volume representation of the imaged radiotracers distribution [2]. In many preclinical systems, filtered back projection is still the dominating analytical algorithm. For practical reasons collected data for all projections are collected into sinograms, containing every projection of a LOR, that is, every angle collected. Many preclinical PET-systems use correction methods known from the clinical systems, such as attenuation correction and scatter correction.

Due to the youth of preclinical PET systems there has been a lack of standardization of their properties. Measurements of such as their spatial resolution and sensitivity have been measured in different ways. NEMA NU 4-2008 *"Performance Measurements of Small Animal Positron Emission Tomographs"* defines a model for how to measure and evaluate the properties of systems in a way that simplifies comparison between systems [32]. Goertzen et al. used the standard on a variety of preclinical PET systems and concludes that one also must consider the suitability of a system for the specific imaging task when considering the results from NEMA testing, since there is a much wider variation in system design in preclinical than clinical PET systems [33].

Method and Equipment

Phantoms

To study how Cerenkov radiation travels through tissue and how its ability to penetrate is limited by the tissues absorption and scattering of the light, a phantom should be constructed with precise optical properties, which gives a chance to quantify the light output.

We designed a simple mouse-sized phantom, measuring 9x3x2 cm, drilled through by five thin channels at increasing depths. Through the channels a silicon tube was inserted. The tube could be filled with a liquid radionuclide, such as [18]FDG. The phantom itself was made of epoxy resin, mixed with toner ink to make it absorbent of light and TiO_2 to make it scatter the light. Epoxy resin has a refractive index of 1.54 [10]. With Equation 2 the threshold energy for a positron to emit Cerenkov radiation was then calculated to 0,161 MeV.
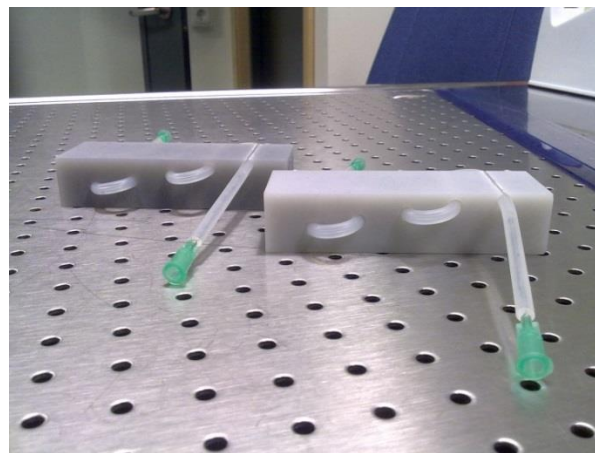

Figure 5 Phantoms made of epoxy resin. When molded, the epoxy resin was mixed with toner ink to make the phantoms absorbent of light by giving them a specific absorption coefficient, and TiO_2 to make the resin scatter light by giving the phantoms a specific scatter coefficient, given in table below.

As a first step, eight phantoms were made, with one transparent phantom (A1) made of pure epoxy resin without any added absorbent or scatter elements. To enable study of the effects on the radiance of absorption and scattering separately, four phantoms had the same absorbing properties (C1, C2, C3 and C4) but different scattering properties. Four of the phantoms had the same scattering properties (A3, B3, C3 and D3) but different absorbing properties.

Table 2 The recipe for the eight phantoms. The epoxy resin was made of a two component mix of a base and a catalyst. The base was measured and the desired amount of ink stock and TiO_2 was mixed with it. To make the resin harden, the catalyst was added. The table states the absorption and scattering coefficient of each phantom.

Phantom name	Total mass (g)	Epoxy base mass (g)	Epoxy catalyst mass (g)	Toner ink mass (g)	TiO_2 mass (g)	μ_a (cm^{-1})	μ_s' (cm^{-1})
A1	210	140	70	0.0	0.0	0.00	0.00
A3	210	140	70	0.0	0.4	0.00	14.74
B3	210	140	67	3.0	0.4	0.11	14.74
C1	210	140	64	6.0	0.0	0.23	0.00
C2	210	140	64	6.0	0.2	0.23	7.37
C3	210	140	64	6.0	0.4	0.23	14.74
C4	210	140	64	6.0	0.8	0.23	29.49
D3	210	140	58	12	0.4	0.46	14.74

After the epoxy resin had hardened, the phantoms were cut to the same size and shape and the channels were drilled. The shallowest channel was milled into the surface of the epoxy resin phantom and light emerging from this channel does not pass through any absorbing or scattering material, except for the walls of the silicon tube in which the radionuclide was injected. The tube had an inner diameter of 0.8 mm and an outer diameter of 4 mm. The rest of the channels are milled into the phantoms at the depths 0.25, 0.5, 0.75 and 1 cm.

Radioactivity

For all measurements made at Lund University Bio Imaging Center (LBIC), both CLI and PET studies, ^{18}F was provided by the Cyklotronenheten at SUS (Skånes univeristetssjukhus). For measurements at the Ahmanson Translational Imaging Division at UCLA, ^{18}F was provided by the UCLA Ahmanson Biomedical Cyclotron Facility.

The CLI-system at Lund University Bioimaging Center

At Lund University Bioimaging Center (LBIC) a novel laboratory-built CLI system is used for fundamental studies of Cerenkov emission from injected mice. It consists of a light-tight box with a CCD-camera mounted on top, looking down towards the floor of the box. The CCD has a wide angle lens, mounted inside the box, to collect light from a wider angle across the bottom of the box. The CCD is connected to a cooling system, lowering the electric noise in the signal. The CCD-camera is directly connected via USB to a computer, making data collection immediate and assessment quick.

Figure 6 Left image: the CLI-box open with dark drapes pulled back. The object meant for imaging is placed at the bottom of the box directly underneath the CCD on the top of the box facing the bottom. A white light image of the object is taken this way and is later used to overlap the CLI images for an anatomical reference. Right image: The CLI-box closed and with the drapes pulled down to shut out ambient light. The CCD is connected to a laptop containing the software controlling its settings. When imaging, the overhead lights in the laboratory are switched of.

The CCD has previously been calibrated with a light source of a known radiance, which makes it possible to directly calculate the radiance from the pixel values of the images. The calibration gives a calibration factor which is included in the MATLAB program OptiScope (described below). During imaging, lights in the laboratory are turned off to minimize ambient light increasing the background level.

Specifications CLI system

Table 3 Specifications of components for laboratory-built CLI-system.

Attribute	Modell
CCD model	Andor iKon-M DU934P-FI
CCD-chip	e2V CCD47-10, 1024x1025 pixels, 13 μm pixels size, 13.3 mm sensor size
Lens	Schneider Kreuznach Xenon f/#0.95, F 25 mm, C-mount
Software	Andor SDK 2.92, Andor SOLIS 4.20

CLI measurements

The phantoms were filled with ^{18}F at the start of each experiment. The activity injected in each phantom came from the same batch, why all phantom tubes contained activity of the same concentration, even if the full tube didn't hold the exact same amount of activity. The measured radiance from a channel would be fitted against the activity in that channel, and as the channels were made to be of the same size, they were assumed to contain the same volume and therefore the same activity. Normally, four phantoms were filled for the same experiment and imaged two and two, by alternating the phantoms placed in the CLI system.

For the phantom studies in this project, the radiotracer-filled phantoms were placed, two at a time, at the bottom of the CLI-system. Images were collected with the CCD. This was set to collect 16 bit gray images for the full data range (0 – 65535). The pixels were binned 4x4, which means the images became 256x256 pixels. The images were collected for a variation of exposure times, 10-600 seconds to enable evaluation of an appropriate exposure time as a function of the activity. Specifically at the beginning of an experiment, while the activity concentration was high, shorter exposure times were used, as the noise level became too high, due to annihilation photons, in images taken with the longer exposure times. As time passed, longer exposure times became necessary to detect the decreasing radiance.

To avoid light scattering and increasing the signal in neighboring channels, the silicone tube was pulled through every second channel, increasing the distance between radioactivity-filled channels. This meant every phantom must be imaged at two different occasions to give data for all channels. Neighboring empty channel would in some cases light up as if filled will radioactivity due to reflections, but at a lower intensity. The intensity profiles over the different channels filled with activity were now separated enough to not overlap.

Images were then collected for the duration of a couple of half-lives of the radiotracer. At the beginning of an imaging session an image was taken as a localization reference. The image was taken while the door to the CLI-system was open. This image was later superimposed on the CLI-image, which made it easier to tell the localization of the light source.
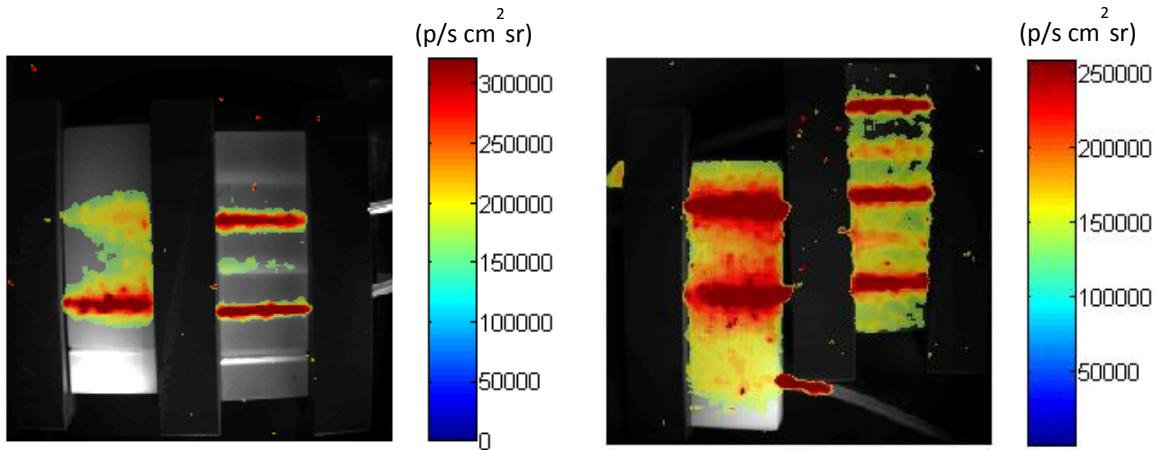
Figure 7 Phantoms A3 and B3 filled with [18]FDG and imaged CLI system at LBIC. Left image: Phantom A3 and B3 imaged with three channels filled with activity. In A3 the empty channels light up as if filled with radioactivity (but as if of a lower activity concentration), due to scattered light reflecting in the channel walls. Right image: phantoms A3 and B3 filled with ^{18}F in the remaining channels not filled in the left image.

Data processing – MATLAB

The images taken with the CLI-system were read and processed with the help of a custom-made MATLAB-program (OptiScope, Johan Axelsson). The program superimposes the CLI-image with the white light imaging. The pixel values of the CLI-images were converted to radiance with the previously known calibration factor. With the program the images can be windowed to visualize the emission from the channels in the phantoms.

To retrieve the radiance from each channel of the phantom, the phantom in the image was marked with a region of interest (ROI). Profiles along the long side of the phantoms were drawn and an average of these was calculated. For each average profile ten lines of pixels were combined. An average profile along the middle of the phantom was chosen.

The maximum radiance from the profile over a channel was picked as measurement of the radiance of that channel. To evaluate the resolution of the CLI-system, the profile over each channel was fitted to a Gaussian function with the help of the MATLAB application Curve Fitting Tool[3]. The application gives the function on the form

$$f(x) = a \cdot e^{\frac{-(x-b)^2}{2c^2}}$$

Equation 19

The full width at half maximum (FWHM) can then be calculated from the term c as

$$\text{FWHM} = c \cdot 2\sqrt{2\ln(2)} \approx c \cdot 2{,}35482$$

Equation 20

With the knowledge of the pixel width in the image, the FWHM could then be calculated.

---

[3] Curve Fitting Toolbox 3.3, Copyright 2001-2012 The MathWorks, Inc.

NanoPET/CT at LBIC

The NanoPET/CT (BioScan) is available at LBIC, and used for small animal imaging of mice and rats. It comprises of 12 detector arrays of LYSO scintillation crystals. It is stated to have a spatial resolution of less than 1.2 mm in the center field-of-view (CFOV) and a sensitivity of 8.3 % at CFOV for an energy window between 250-750 keV [34]. The system has a field-of-view (FOV) of 100x94 mm.

Figure 8 The NanoPET/CT at LBIC.

Reconstruction is done with an iterative 2D OSEM algorithm.

Siemens Inveon

At the Ahmanson Translational Imaging Division at UCLA, the Inveon microPET (Siemens) system is used for small animal imaging. The system uses LSO scintillation crystal detectors and has according to the manufacturer a resolution (FWHM) in the CFOV of 1.4 mm [35].
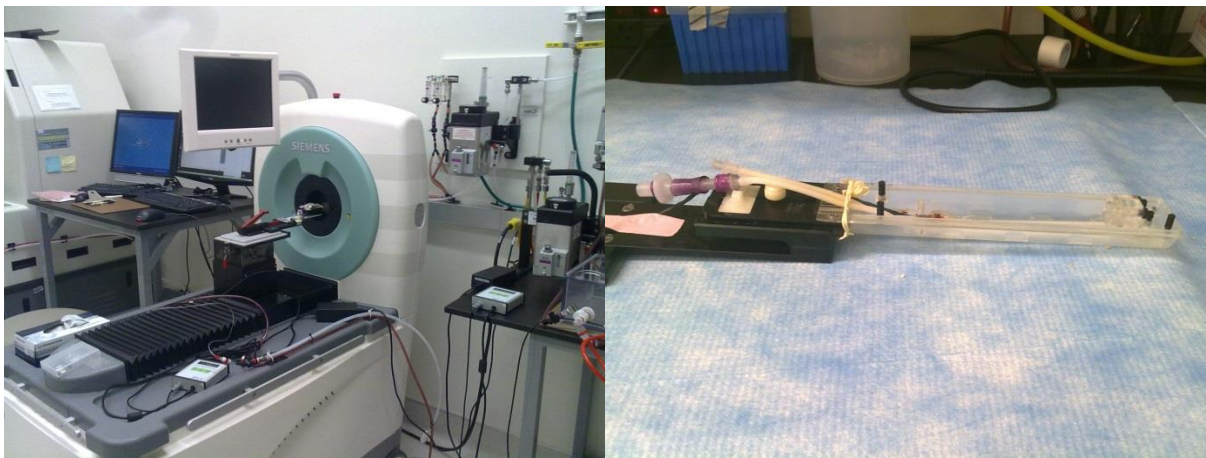

Figure 9 Left image: The Inveon PET-system (Siemens) at the Ahmanson Translational Imaging Division at UCLA.

Right image: the PET-systems mouse cradle in which the phantoms where mounted during the scan.

The sensitivity is greater or equal to 10 % at the CFOV [35].

The reconstruction is made with an iterative OSEM algorithm.

Genisys4 Table Top PET

The Genisys4 (Sofie Biosciences) differs from most preclinical PET system in that it consist of four detector panels, instead of multiple detectors as in detector ring PET scanners. This gives it different properties, even though the basic idea of detecting true coincidences is still there.

A first basic description of the system and its performance was given by Gu et al [36]. They described the precursor to the Genisys4, the PETBox4, as consisting of four opposing detector panels arranged in a box like geometry. Each panel is made by a 24 x 50 array of 1.8 x 1.8 x 7 mm BGO scintillation crystals. Each panel is coupled to two PM-tubes via a glass light guide. The FOV is 4.5 cm in a transaxial direction and 9.4 cm in the axial direction. The system uses a MLEM algorithm to reconstruct images. The system has an X-ray system for reference images and attenuation corrections.

To evaluate the system performance, Gu et al. measured the sensitivity with a drop of ^{18}F placed in the CFOV [36]. With an energy window between 150 - 650 keV and a timing window of 20 ns the peak sensitivity was found to be 14%, which is quite high compared to conventional preclinical PET scanners. The spatial resolution was measured with a ^{22}Na point source. The intrinsic spatial resolution was found to be 1.5 mm in both axial and transaxial directions. The reconstructed spatial resolution was on average 1.46 mm.

The performance of Genisys4 has been evaluated and compared to other preclinical PET scanners by Bai et al[37]. The comparison was made with the first generation of commercial scanner microPET R4 and its latest generation scanner Inveon (Siemens). It should be noted that scatter correction wasn't available for Genysis4 but for the two conventional scanners. Bai et al. came to the conclusion that Genisys4 had a resolution comparable to the other scanners, but that its images had an increased background activity [37]. A reason for this might be the quite wide energy window, which will allow a lot of scatter events to be detected as coincidences. This could be minimized with scatter correction. Bai et al also noted that Genisys4 could provide high quality images with activities as low as 37 kBq.

The system was further evaluated by Hermann et al [38]. They compared the system's ability to detect subcutaneous xenographs and lung metastases with that of an established preclinical PET. They found the Genisys4 to detect these equally well as the established system.

At the Ahmanson Translational Imaging Division at UCLA the Genisy4 is used for small animal imaging.

Figure 10 Left image: The Genisys4 PET-system (Sofie BioSciences) at the Ahmanson Translational Imaging Division at UCLA. Right image: the PET-systems mouse cradle in which the phantoms where mounted during the scan.

33

Data collection for the PET-systems

For all three PET-systems (Siemens, BioScan and Sofie Biosciences), dynamic measurements were made, imaging one of the phantoms filled with ^{18}F in all the channels. For the Genisys4 and the Inveon, measurements were made by five minutes dynamic data collection for a number of hours. Several images where analyzed and the best results are presented below. For the measurement with the NanoPET/CT at LBIC a 20 min dynamic study was made.

To evaluate the spatial resolution of the measurements, the same technique as that used to evaluate the FWHM for the CLI images was used. Profiles over the channels where fitted to a Gaussian curve with the MATLAB application Curve Fitting Tool[4]. The term c (from Equation 19) given by the fitting tool was used to calculate the FWHM from Equation 20.

The sensitivity was evaluated by comparing the number of prompt coincidences measured during the dynamic scan to the calculated number of decays from the known activity in the phantom. The quota gives the sensitivity in %.

---

[4] Curve Fitting Toolbox 3.3, Copyright 2001-2012 The MathWorks, Inc.

Results - CLI

The radiance from each channel of the different phantoms was analyzed with the MATLAB program OptiScope (described above) for a large number of images collected over a couple of hours during which the ^{18}F decayed. As the activity decays, it gives an opportunity to measure the radiance from decreasing activities in the channels.

Radiance vs. activity of ^{18}F

In Figure 11 a representative plot of the radiance from the five channels in phantom A3 is plotted as a function of the activity concentration of ^{18}F in the channels. All phantoms show the same trend and all give support to the same theoretical expectations.
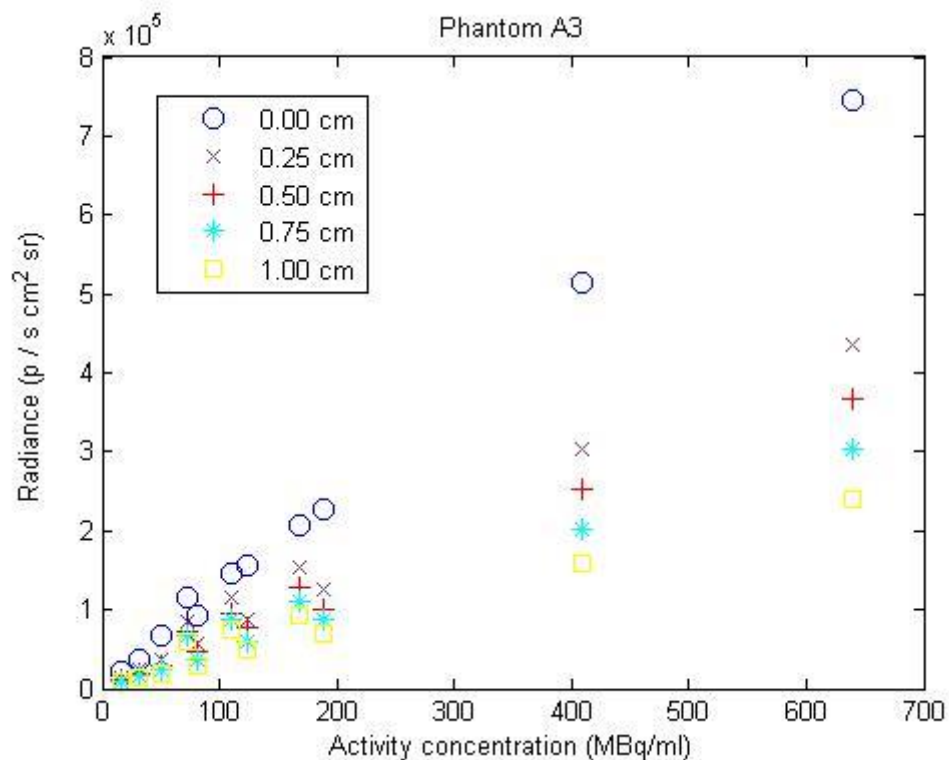
Figure 11 The radiance from all channels in phantom A3 plotted as a function of the activity of ^{18}F in the channels. The radiance deceases with a decreasing activity. The radiance is consistently lower for deeper lying channels.

The trend of an increasing linear relationship between activity and radiance is consistent throughout all channels in all phantoms. This is an expected result related to the theory and the description of the origin of Cerenkov radiation.

In the Frank Tamm formula in Equation 4 and Equation 5, the energy of the Cerenkov radiation emitted by a charged particle is described. These equations states that the light is emitted as a continuous spectrum. All charged particles with sufficient energy will emit light with the same spectral distribution; higher energies will raise the intensity. In a similar way the energy distribution for emitted positrons from ^{18}F does not change when the activity is increased, it will only increase the intensity. As the activity increases so does the flux of positrons with sufficient energy to emit Cerenkov radiation. More positrons emitting Cerenkov radiation will lead to an increase in the total amount of light emitted and a larger radiance detected.

35

These plots also show a decreasing radiance with increasing depth. Cerenkov radiation produced deeper inside the phantom must travel a longer distance and will then be more affected by the absorbing and scattering properties of the phantom. This is consistent with the theoretical description of the radiance decreasing as a function of the distance R traveled through a material of the effective attenuation coefficient μ_{eff} as described in Equation 14.

Radiance vs. absorption coefficient

The radiance of the four phantoms with the same scattering properties but varying absorption coefficients (A3, B3, C3 and D3, see Table 2) is plotted as a function of the activity of ^{18}F in each channel. One plot is made for each depth of the channels. A linear function is fitted to each data series.

For the depths 0.25-1 cm a clear decrease in the slope of the linear relationship between radiance and activity is seen for an increasing absorption coefficient. This is shown for the depth 0.25 cm in Figure 12 below. The depths 0.5-1 cm are not shown but display the same relationship between absorption coefficient and the slope of the linear function.
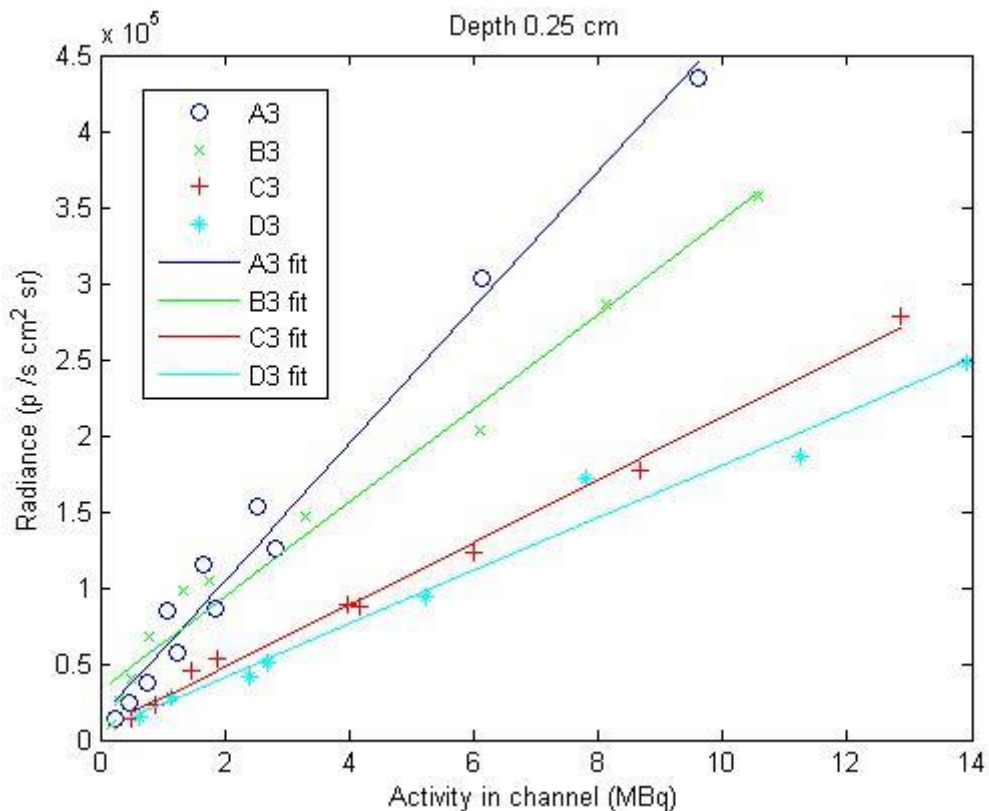

Figure 12 The radiance measured form the channels at the depth 0.25 cm plotted aginst the avtivity of ^{18}F in the channes. The radiance deceases from phantoms with a higher absorption coefficient.

For the depth 0 cm the radiance is expected to be decreased with decreasing activity of ^{18}F, according to the same linear relationship for all phantoms. This channel is at the surface of the phantom and the emitted Cerenkov radiation should all be from the silicon tube. But due to scattering in the channel walls and variations in the exact position of the drilling of the channel, the radiance varies in an inconsistent way between the four phantoms, as can be seen in Figure 13 below.
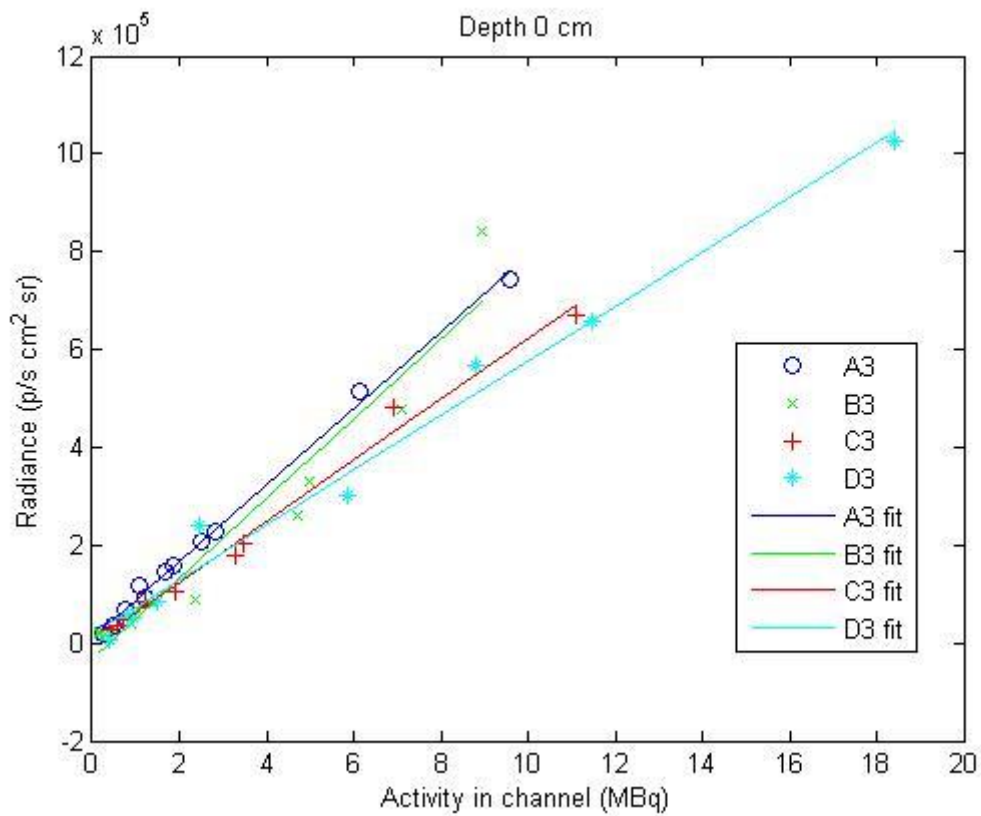
Figure 13 The radiance from the four phantoms with varying absorption coefficient at the most shallow channel.

The fitted linear functions for the four different values of absorption coefficient are used to calculate the radiance as a function of absorption coefficient for a variety of ^{18}F activities. Below in Figure 14 the radiance is plotted for an activity of 3 MBq ^{18}F in the channels.
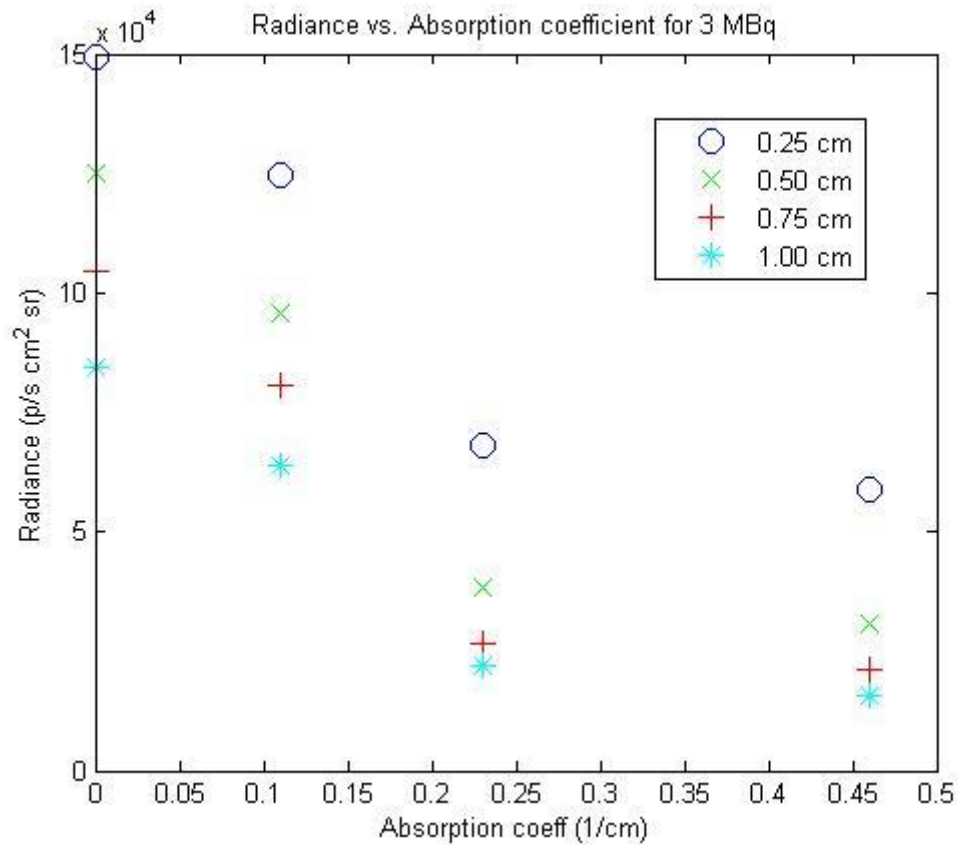
Figure 14 The radiance of Cerenkov radiance has a decreasing relationship to an increasing absorption coefficient.

In Figure 14 a clear decreasing relationship between radiance and increasing absorption coefficient is apparent. This is, as described for Figure 12, an expected result from the theory, in accordance with Equation 14.

Radiance vs. scatter coefficient

The four phantoms with varying scatter coefficient (C1, C2, C3 and C4, see Table 2) are plotted for each depth of the channels. Below in Figure 15 the radiance for the channel at the depth 0.50 cm is shown, and a linear function is fitted to the data from each phantom.
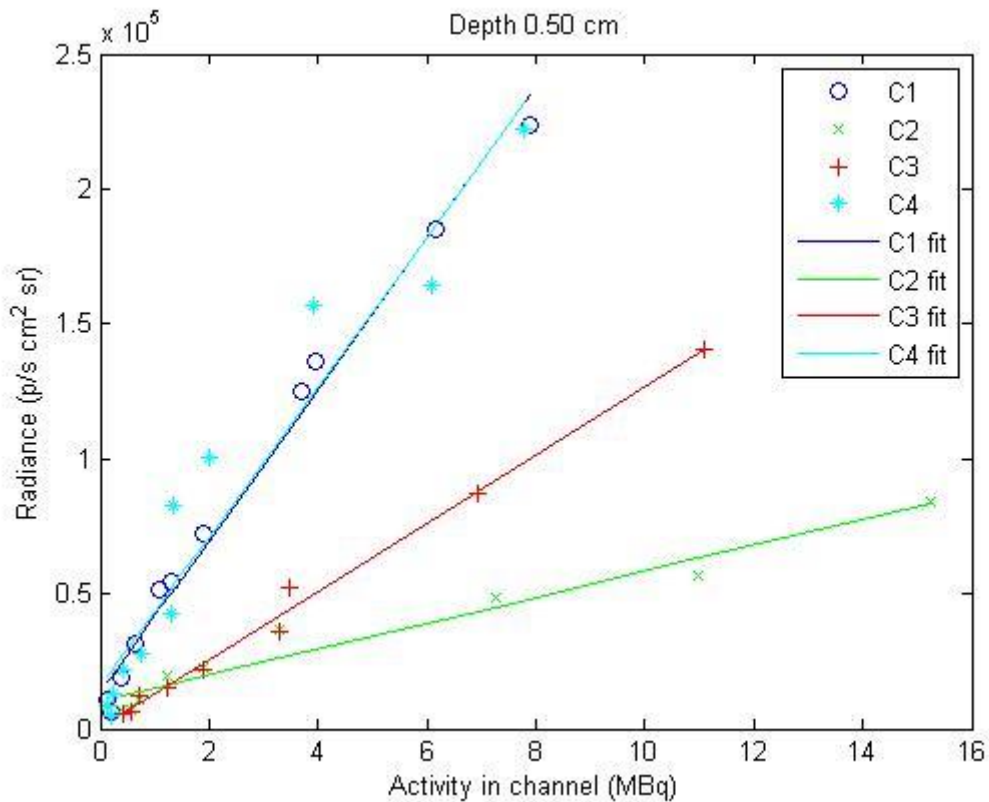
Figure 15 The radiance as a function of activity of ^{18}F in the channels at the depth 0.50 cm in the four phantoms with varying scattering coefficient. With exception for phantom C1 without any added scattering TiO$_2$ and therefore a theoretical scattering coefficient of 0 cm^{-1}, the slope of the fitted linear functions increases as the scattering coefficient increases.

The plotted data in Figure 15 shows the same trend for all depths (0.25 - 1.00 cm) of the four phantoms. Excluding phantom C1, the plots show an increasing inclination to the fitted functions for an increasing scattering coefficient. With a higher scattering coefficient, the light traveling through a material can propagate longer distances due to a greater number of scattering events. As the scattering coefficient is increased, more light is scattered up to the surface.

But, enough scattering can also dampen the light radiance as it is scattered into a bigger volume of the phantom. And during the longer distance travelled by the light, a larger number of absorptions will occur. This can explain why phantom C1 displays a level of radiance comparable to phantom C4. When going from no scattering to the lowest level examined in this study, the light is reduced in the forward direction due to scatter. As the scattering level is increased more light emitted in the opposite direction from the surface can be scattered all the way to the surface and we get an increasing radiance. If phantoms with even higher scattering coefficients had been made, a possible observation could have been a point at which the radiance starts to decrease due to "too much" scatter.

Linear functions are fitted to the data series in Figure 15 and used to calculate and plot the radiance as a function of the scattering coefficient. This is done for an activity of 3 MBq in the channels and plotted for the different depths of the channels in Figure 16.
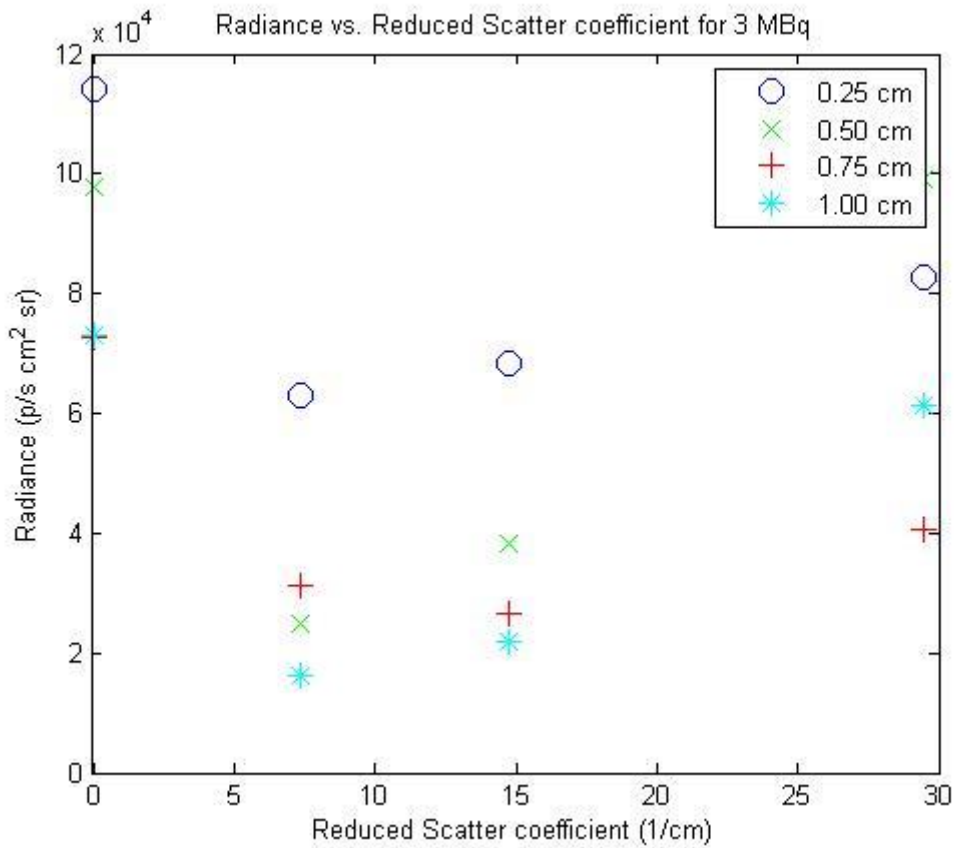
39

Figure 16 The radiance from the channels of different depths in the phantoms plotted as function of the scatter coefficient. With the exception of the data points for a scatter coefficient of 0 cm^{-1} an increasing trend for increasing scatter coefficient.

If excluding the data points from the lowest scattering coefficient (0 cm^{-1} in phantom C1), a trend of increasing radiance with increasing scattering coefficient can be observed. It seems as if the highest scattering coefficient plotted has its biggest impact on the deeper situated channels, as these become more separated in the plot.

FWHM vs. depth

The phantom A1 has no additives to give it any scattering or absorbing properties. Therefore it is used to study the effects of depth independent of scattering and absorption. The measured FWHM as a function of depth is plotted in Figure 17 below.
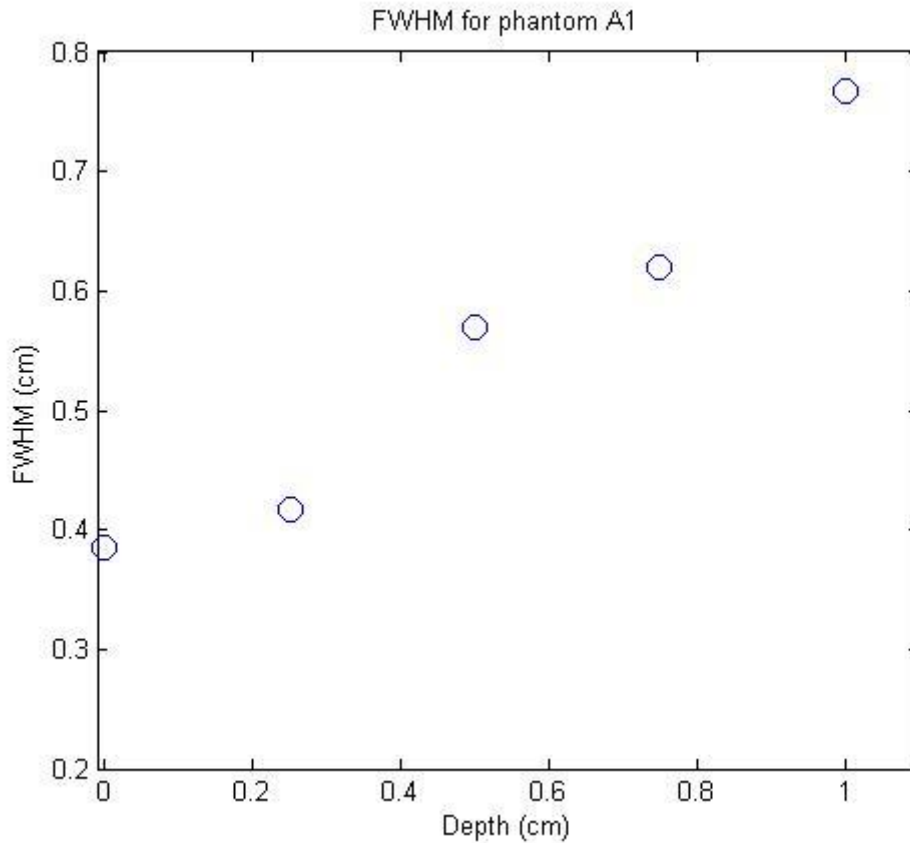
Figure 17 The influence of depth on FWHM independent of scattering and absorption.

An increasing trend is observed between FWHM and depth.

FWHM vs. absorption coefficient

The FWHM is analyzed from the data of the phantoms with varying absorption coefficient (A3, B3, C3 and D3, see Table 2) for different depths of the channels. Linear functions are fitted to the data. The linear functions found through the regression are then used to calculate the FWHM for a variety of depths. The result is given in Figure 18 below.

A trend of decreasing FWHM with increasing absorption coefficient is seen in Figure 18 below. This is explained from the fact that a higher absorption coefficient will attenuate photons that travel long path lengths through the tissue. This renders a more narrow intensity distribution at the surface, i.e. a smaller FWHM.
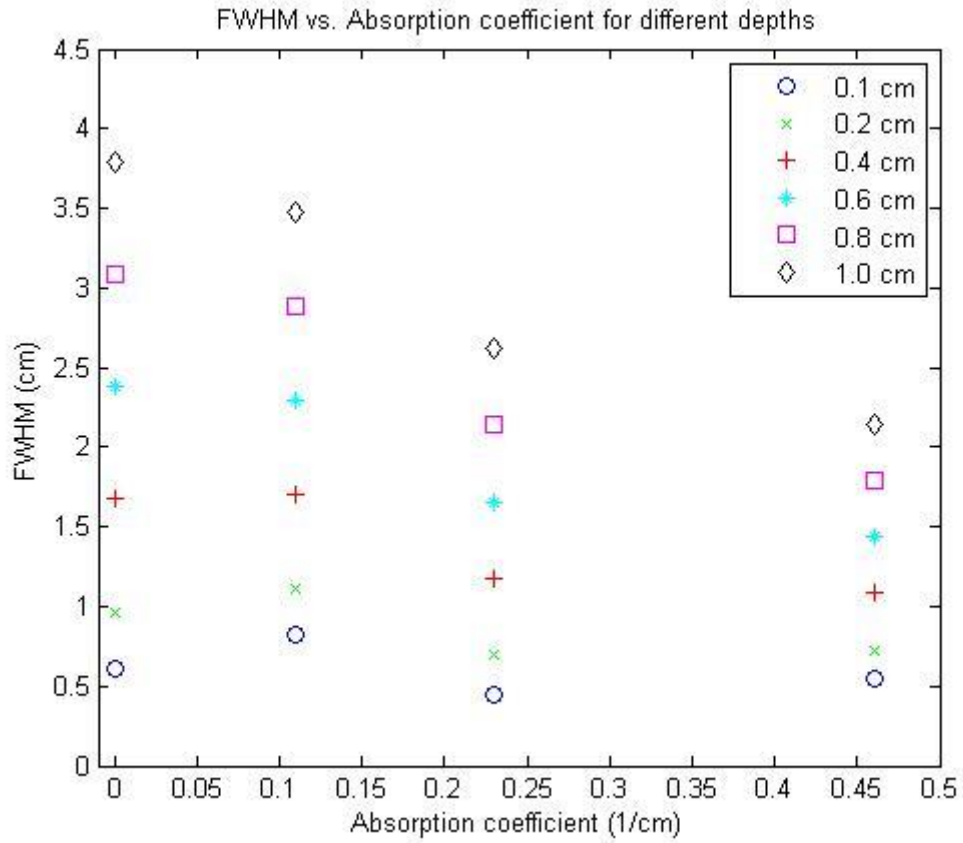
Figure 18 The FWHM plotted as a function of the absorption coefficient for a variation of depths. A decreasing radiance with an increasing absorption coefficient is observed.

FWHM vs. scattering coefficient

For the four phantoms with varying scattering coefficient (C1, C2, C3 and C4, see Table 2), the FWHM is analyzed as a function of the depth of the channels (not shown). Linear functions are fitted to the data points. These are used to calculate the FWHM for different depths and are plotted below in Figure 19.
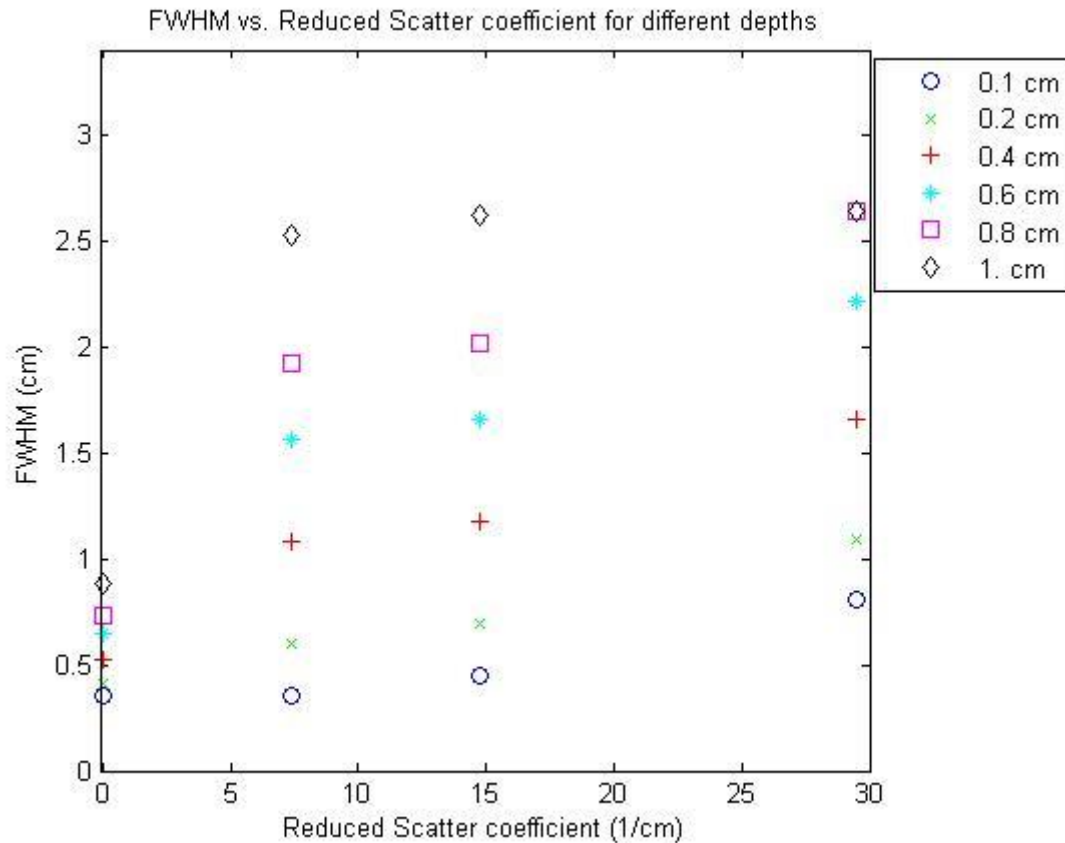
Figure 19 The FWHM at the surface of the phantoms as a function of the scatter coefficient plotted for a variation of depths. An increasing FWMH with an increasing scatter coefficient is observed.

A vague trend of an increasing FWHM with increasing scattering coefficient can be observed. This is consistent with the theoretical expectations, a highly scattering material will broaden the profile of the light emitted as it is scattered over a wider angle, and therefore giving a broader FWHM.

In both Figure 18 and Figure 19 we see an increasing FWHM as the depth of the source is increased. As the light travels longer distances, more scattering events occur and the profile therefore broadens.

The data points from $\mu_s' = 0$ cm^{-1} differs from the trend of the other. These originate from the linear fit from the FWHM data from phantom C1. Since the tubes outer diameter is 4 mm, we expect a FWHM in the vicinity of this value if there is no scattering. The points therefore seem to be in consistence with the expected result.

Results - PET

From the three measurements made on the three different PET-systems (Genisys4 (Sofie BioSciences), Inveon (Siemens) and NanoPET/CT (BioScan)) the FWHM and the sensitivity has been calculated as described above. The results are presented in Table 4 and Table 5 below.

43

FWHM

Table 4 The measured FWHM from the dynamic measurements made on the PET-systems Genisys4 (Sofie BioSciences), Inveon (Siemens) and NanoPET/CT (BioScan). The smallest FWHM and therefore best spatial resolution is given by the NanoPET/CT (BioScan).

PET-system	FWHM (cm)	FWHM (CFOV) according to manufacturer (cm)
Genisys4	0.24	0.14
Inveon	0.20	0.14
NanoPET/CT	0.18	0.12

Sensitivity

Table 5 The measured sensitivity from the dynamic measurements made on the PET-systems Genisys4 (Sofie BioSciences), Inveon (Siemens) and NanoPET/CT (BioScan). The highest sensitivity is given by the Genisys4 system (Sofie BioSciences).

PET-system	Measured sensitivity (%)	Sensitivity according to manufacturer (%)
Genisys4	5.9	14
Siemens Inveon	1.4	10 (CFOV)
NanoPET at LBIC	3.5	8.3 (CFOV)

Discussion

CLI

Throughout this thesis, the results have shown a basic consistency with the fundamental theory of the origin of Cerenkov radiation and the attenuation of optical light in tissue. It is evident that Cerenkov radiation is affected by both absorption and scattering in different ways. Employing the phantom set, developed within this work, it is possible to investigate the impact of depth, absorption and scattering separately.

Cerenkov radiance vs. activity

Figure 11 showed an increasing radiance as a function of activity in the channels. This is logical consequence, since a higher activity of ^{18}F causes a higher radiance. The higher activity gives rise to a higher flux of positrons in the channels and the phantom, emitting the Cerenkov light. This is consistent with the results presented previously by many, including the initial study on CLI by Robertson et al [12].

During the CLI measurements, it was noted that high activity and long exposure times resulted in very noisy images. For phantoms of a high effective absorption coefficient this noise was enough to drown the signal from the deeper channels. The noise is assumed to be due to high energy photons, such as the annihilation photons or secondary Compton scattered photons, hitting the CCD and "killing" pixels by saturating them. A shorter exposure time will limit the noise, since fewer pixels will be saturated before the shutter is closed. Intuitively, a lower activity will give a lower noise level, since the flux of annihilation photons and its progeny from interactions are directly proportional to it.

During imaging, it was noted that empty channels in the phantoms lit up due to reflections, as showed in Figure 7. The radiance from these channels was ignored and never measured. But it still raises the question whether similar reflections in tissue could create false sources of light. It could potentially happen in cavities such as lungs, but would probably not be a problem in denser tissues.

Influence of depth (radiance and resolution)

Figure 11 also showed the impact of depth in the phantom, indicating the effective attenuation of light as it passes through the phantom. The radiance detected at the surface is therefore dependent on the distance the light has travelled as described by Equation 14. This shows consistency with the previously mentioned work by Park et al, showing the smallest activity concentration of ^{124}I detectable with CLI after injection in the back muscle of rats increased for growing depths [20].

In Figure 18 and Figure 19 the influence of depth on the resolution becomes evident. As the depth is increased the FWHM is broadened. The FWHM, depending on depth and phantom, varied between 0.4 - 3.8 cm, a very large span. The biggest variation of FWHM calculated for the depths 0.1 - 1.0 cm within the same phantom was found for phantom A3 which showed a FWHM span of 0.6 - 3.2 cm. In the previously mentioned study by Liu et al, a spatial resolution of 1.2 mm for CLI using ^{18}F was measured [14]. This is obviously a large difference to the results of this thesis, but it is clearly due to the different methods used. Liu et al used a Micro Deluxe phantom, normally used for spatial resolution assessments for established nuclear imaging modalities, and not a line source like the channels in this study's phantoms. There measurement did not take depth, absorption and scattering into account for the potential spatial resolution of CLI [14].

45

When light travels longer distances through a scattering medium it will be subjected to more scattering events, all widening the distribution of the light. All phantoms (except C1 and A1, A1 is not contributing with any data in these results) have a scattering component. This includes the four phantoms with varying absorption coefficients (A3, B3, C3 and D3).

Phantom A1, as can be seen from Table 2, has no additives to give it any scattering or absorbing properties. The FWHM measured for the depths of the channels is plotted in Figure 17. A small broadening of the FWHM is seen for greater depths. This implies that the FWHM is a function of depth independent of the scattering and absorbing properties of the medium. This is in consistency with the inverse square law, since the sphere area A of the light distribution has a $A \propto r^2$ relationship to the radius r. The radius is here the distance from the channel to the surface. As the area of the sphere is increased, the angle at which the light hits the surface is also increased. From the law of refraction it is evident that if the incident angle of a ray is increased, so is the angle of the refracted ray. This leads to a broadening of the FWHM.

The depth of an activity uptake will inevitably limit the chances to detect and quantify it. It will appear broader, due to the larger FWHM, and less radiant, due to the divergence and absorption of the light.

Influence of absorption (radiance and resolution)

The impact of the absorption coefficient on radiance is investigated in Figure 12 to Figure 14. A 100 % increase of absorption coefficient from 0.11 cm^{-1} to 0.23 cm^{-1} reduced the radiance by 60 % from the channel at depth 0.5 cm when filled with 3 MBq ^{18}F. The decreasing radiance for an increasing absorption coefficient is due to greater light absorption which can be theoretically described by the effective attenuation coefficient in Equation 13.

The relationship studied is according to the theory in Equation 14 an exponentially decreasing relationship. Exponential functions could be fitted to the data in Figure 14 with accuracy R^2 between 0.85-0.88 for the four different data groups. A better fit could possibly been made if the radiance had been plotted against the effective attenuation coefficient rather than the absorption coefficient. If scattering could be considered negligible the radiance could be described by the Beer-Lambert law, Equation 11, but since the phantoms used for evaluating the absorption all have a scattering component, Beer-Lambert law is not valid.

In Figure 18 the FWHM showed a decreasing trend for an increasing absorption coefficient. When the intensity profile of the light propagates through the medium it will attenuate it in accordance with the absorption coefficient of the medium. The fading, less intense radiance at the wings of the profiles will be absorbed. The profile will therefore become narrower for each unit length it travels through the medium.

Absorption will more than the other factors limit the sensitivity of a CLI-system.

Influence of scattering (radiance and resolution)

Figure 16 shows an increasing radiance as an effect of an increasing scattering coefficient. A 100 % increase of scattering coefficient from 7.37 cm^{-1} to 14.74 cm^{-1} increased the radiance with 54 % from the channel at depth 0.5 cm when filled with 3 MBq ^{18}F. This is a slightly more complex relationship than that seen for the absorption coefficient, since the effect of scattering could both be expected to raise the measured radiance and lower it. The scattering properties of the material can scatter light

not travelling towards the surface to change its direction sufficiently to reach the surface. But, it will also have a reducing affect as the scattered light travels a longer distance and therefore is more absorbed along the way to the surface.

As mentioned in the results for Figure 15, the radiance measured for phantom C1 is not actually subjected to any scatter since it has no added TiO_2 giving it scattering properties. The radiance measured is attenuated due to the absorption coefficient of the phantom and the distance travelled through it. The scattering of the remaining phantoms probably lowers the intensity due to the longer distance travelled through an absorbing medium, compared to the distance travelled by the light photons in phantom C1. As the scattering coefficient is increased, more light is scattered towards the surface and the radiance from the most scattering phantom (C4) reaches a level comparable to that of C1. It is plausible that the attenuating effects due to the longer distance travelled could have more impact for even higher scattering coefficients. If phantoms with even higher scattering coefficients had been made, we might have observed a point at which the radiance falls due to increasing scattering. Unfortunately no time was found within the scope of this project to construct more phantoms. The phantoms constructed were designed to cover the commonly found absorbing and scattering coefficients found in biological tissue.

In Figure 19 the FWHM showed a trend of broadening as the scattering coefficient increased. This is consistent with theoretical expectations. When light is scattered its intensity profile is broadened. Similar to previous plots, the data points for $\mu_s' = 0$ cm^{-1} did not really follow the trend of the other points. These data points come from the measurements of the FWHM from phantom C1, which as described in the previous paragraph has not been subjected to any scattering. The absorption coefficient of the phantom is expected to narrow the profiles of the light and this is the same for all four phantoms.

CLI for quantitative longitudinal studies

Since CLI is influenced by optical properties it can't be directly used for quantitative studies. For this to become possible some form of attenuation correction would be needed. Such a correction is achieved in conjunction with CLT, using additional light sources, but will undoubtedly lead to longer examination times. Another approach would be to assess the effective attenuation coefficient separately using an external light source.

The main motivation for developing such attenuation correction scheme is that the optical properties can very likely change during the course of treatment. Most importantly the absorption properties due to blood, since changes in vascularity and oxygen saturation are probable responses to radiation therapy. It has been shown that vascularity, blood volume and blood flow can change significantly as a response to radiation therapy [39, 40]. An increasing blood flow and blood volume would increase the effective attenuation coefficient. If this happens fast and at a sufficient rate, i.e. during the duration of a mouse participation in a study, it will perturb the measured radiance.

The two studies quoted above are from human and canine subjects. It is likely that the response to radiation therapy is strongly dependent on tumor type. Similar studies have been made for mice.

Fujii et al. studied the oxygen partial pressure for a squamous cell carcinoma bearing animal model following external beam radiation therapy. It was seen that the oxygen content in the tumor

increased rapidly and then decreased slowly to pre-irradiation levels within less than two weeks. A lower absorbed dose rendered a faster return to pre-irradiation oxygenation [41].

Vishwanath et al. studied the oxygen saturation following external radiation therapy of a murine animal model inoculated with head and neck cancer cells. The results indicated a gradual increase in oxygen saturation from 5 to 17 days post irradiation. However, they did not see any changes in the blood volume. This finding is important since a constant blood volume will keep the average absorption coefficient the same whereas the change in oxygen saturation will only change the absorption spectrum of hemoglobin, rendering only small changes in the effective attenuation coefficient across the visible spectrum [42].

These two studies indicate, by proving changes in oxygen content in tumors and oxygen saturation of blood but not blood volume, that there are changes in optical properties during radiation therapy. However, the changes are mostly due to oxygenation changes and the total optical absorption seems to be more or less constant.

To visualize the difference in impact on the absorption between oxygenation and change in blood volume, the absorption coefficient can be calculated from Equation 12. This is done by using the extinction coefficients of oxy- and deoxygenated blood. The result is plotted in Figure 20.
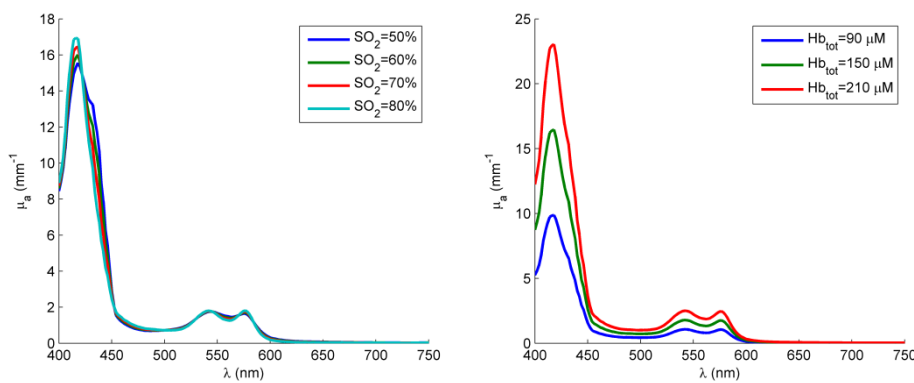

Figure 20 Left image: the absorption coefficient as a function of wavelength for four levels of oxygen saturation. Right image: the absorption coefficient as a function of wavelength for three levels of blood volume.

The influence of these small changes in absorption spectrum is moderate when studying superficially emitted Cerenkov radiance, as indicated by the results in this thesis, as well as previously reported publications that has shown good correlation between CLI and PET measurements of shallow activity uptakes in vivo [15, 18, 21]. However, a deeper lying Cerenkov emitter will be more affected, rendering a need for attenuation correction of the emitted light.

On the other hand, due to the influence of optical properties, there are possible means of using the Cherenkov emission for analysis of the tissue or tumor physiology. Changes in emitted Cerenkov radiation could potentially indicate oxygenation of hypoxic tumor cells, or shrinkage of the whole tumor volume from changes in light propagation depth.

Positron Emission Tomography

FWHM

The results in Table 4 show a slightly broader FWHM for all PET-systems compared to the FWHM reported by the manufacturers. These measurements are not optimized for FWHM evaluation. FWHM measurements are, according to the NEMA NU-2008 standard, preferably made with a ^{22}Na point source [32]. Instead we used several line sources within a phantom filled with ^{18}F. Our phantoms were constructed with the CLI measurements in mind, and did not intend to make spatial resolution measurements to fully evaluate the PET systems, but to give a comparison to the CLI measurements of the same geometry.

The best resolution of the systems is given by the NanoPET/CT system, which has the best stated resolution out of the three systems, according to the manufacturers.

Sensitivity

The results in Table 5 show a rather large difference between the sensitivities measured and the ones stated by the manufacturers for all the systems tested in this thesis. But, it points to a similar relationship of capacity between the different systems, with the Genisys4 giving the best sensitivity.

But again, the method used is not the NEMA NU-2008 standard [32]. Sensitivity should according to the standard be measured with a ^{22}Na point source placed at the CFOV. In this case the activity is not a point source but spread out over most of the FOV. Also, the standard states that the reconstruction should be made with a filtered back projection. These systems used different versions of iterative reconstruction algorithms.

PET vs. CLI

These preclinical PET measurements were not made to show the sensitivity and spatial resolution at optimal conditions, but to offer a comparison for the CLI measurement. Since the sensitivity and FWHM depends on different factors for PET and CLI, the phantoms were made with the CLI-measurements in mind and did not consider the PET measurement more than to make sure the phantoms would fit in the different PET-systems.

The sensitivity in PET gives a correlation to its ability to quantify activity uptake. Since the number of expected coincidences is directly a function of activity, quantifications can easily be done with a high accuracy in PET. For CLI the radiance does not have the same direct relationship to activity and we cannot really calculate the sensitivity as a property for CLI. It would, as discussed above, take some form of normalization for the optical properties.

The spatial resolution is also dependent on different factors for CLI and PET, but can still be measured in a suitable way for CLI. A big difference between the two modalities is the depth dependence for the FWHM in CLI. The high energy annihilation photons are slightly attenuated through the phantoms but most systems apply scatter and attenuation corrections. It also won't make a big difference between oxy- and deoxygenated blood, but will be equally attenuated by both. We therefore see a big variation of FWHM for CLI from down to 4 mm up to a few centimeters for deeply situated channels in highly scattering phantoms. The PET systems on the other hand can be trusted to resolve structures down to a few millimeters.

The CLI-system will never challenge preclinical PET as a quantitative modality, but do pose an opportunity for imaging schemes taking advantage of both modalities' benefits. Quantitative PET and effective attenuation coefficient assessment at the starting point of a longitudinal study could enable tumor model assessments with CLI, with PET providing tumor uptake validation and effective attenuation coefficient assessment offering a way to normalize the Cerenkov radiance for activity uptake. Using a combined imaging approach would decrease the machine time for PET imaging since the number of PET scans is reduced. Here CLI could find a place for serial imaging of radionuclide uptake in subcutaneous tumors. The method of this thesis could potentially form the foundation for a standard quality assessment method for CLI. Like preclinical PET has the NEMA NU-2008 standard giving directions for quality assessment, CLI if used for preclinical studies, would need standards for evaluation of the imaging technique quality to make studies comparable. The method could include schemes for evaluating the imaging properties of new radionuclide compounds in a standardized way, potentially with phantom studies similar to those performed in this thesis.

Conclusion

This thesis has investigated the potential of CLI as a new preclinical imaging modality. The results pointed out the need for effective attenuation coefficient assessment as an initial step in longitudinal studies and the limits of what depths could be correctly imaged. CLI lack the ability to perform quantitative uptake measurements, but benefits from quick image acquisition with a direct readout of radiance without need for tedious image reconstruction. In combination with quantitative PET, CLI could be part of a longitudinal imaging scheme where serial CLI measurements reduce the need for repeated PET imaging.

The method of this thesis could also form the foundation for a standard quality assessment method for CLI. Like all imaging modalities, CLI needs a standard for evaluation of the imaging technique quality. The method could include schemes for evaluating the imaging properties of new radionuclide compounds in a standardized way with phantom studies similar to those performed in this thesis.

CLI will not take the place of already available preclinical imaging modalities such as PET and SPECT, as it is unable to perform quantitative uptake measurements on its own. But it can become a compliment in future longitudinal imaging schemes, lowering the machine time needed for PET or SPECT and adding a faster and less complicated technique for serial imaging.

References

1.	de Kemp, R.A., et al., *Small-Animal Molecular Imaging Methods.* The Journal of Nuclear Medicine, 2010. **51**(5).
2.	Ziegler, S.I., *PET and SPECT*, in *Small Animal Imaging*, F. Kiessling and B.J. Pichler, Editors. 2011, Springer-Verlag: Berlin Heidelberg.
3.	Jelley, J.V., *Cerenkov radiation and its applications*. Vol. 227. 1955: Pergamon Press London.
4.	Spinelli, A.E., et al., *Cerenkov radiation allows in vivo optical imaging of positron emitting radiotracers.* Physics in Medicine and Biology, 2010. **55**: p. 483-495.
5.	Mitchell, G.S., et al., *In vivo Cerenkov luminescence imaging: a new tool for molecular imaging.* Philosophical transactions. Series A, Mathematical, physical, and engineering sciences, 2011. **369**(2011): p. 4605-19.
6.	Schulz, R.B. and V. Ntziachristos, *Optical Imaging*, in *Small Animal Imaging*, F. Kiessling and B.J. Pichler, Editors. 2011, Springer-Verlag: Berlin Heidelberg.
7.	Dothager, R.S., et al., *Cerenkov radiation energy transfer (CRET) imaging: a novel method for optical imaging of PET isotopes in biological systems.* PLoS One, 2010. **5**(10).
8.	Douraghy, A. and A.F. Chatziioannou, *Preclinical Imaging*, in *Basic Sciences of Nuclear Medicine*, M.M. Kahalil, Editor. 2011, Springer-Verlag.
9.	Axelsson, J., *Model-based Approaches to Diffuse Optical Imaging and Dosimetry*, in *Division of Atomic Physics, Department of Physics,* 2009, Lund University
10.	Pogue, B.W. and M.S. Patterson, *Review of tissue simulating phantoms for optical spectroscopy, imaging and dosimetry.* Journal of Biomedical Optics, 2006. **11**(4).
11.	Cho Jennifer S , T.R., Olma Sebastian, Liu Kan, Chen Yi-Chun , Shen Clifton K-F, van Dam R Michael and Chatziioannou Arion F, *Cerenkov radiation imaging as a method for quantitative measurements of beta particles in a microfluidic chip.* Phys. Med. Biol., 2009. **54 (2009)** p. 6757–6771.
12.	Robertson, R., et al., *Optical imaging of Cerenkov light generation from positron-emitting radiotracers.* Physics in medicine and biology, 2009. **54**(2009): p. N355-65.
13.	Beattie, B.J., et al., *Quantitative modeling of Cerenkov light production efficiency from medical radionuclides.* PloS one, 2012. **7**(2): p. e31402-e31402.
14.	Liu, H., et al., *Molecular optical imaging with radioactive probes.* PLoS One, 2010. **5**(3).
15.	Ruggiero, A., et al., *Cerenkov luminescence imaging of medical isotopes.* Journal of Nuclear Medicine, 2010. **51**(7): p. 1123-1130.
16.	Ackerman, N.L., Graves, E. E., *The potential for Cerenkov luminescence imaging of alpha-emitting radionuclides.* Physics in medicine and biology, 2012. **57**(3): p. 771-83.
17.	Thorek, D.L., et al., *Cerenkov imaging - a new modality for molecular imaging.* Am J Nucl Med Mol Imaging, 2012. **2**(2): p. 163-173.
18.	Robertson, R., et al., *Multimodal Imaging with 18F-FDG PET and Cerenkov Luminescence Imaging After MLN4924 Treatment in a Human Lymphoma Xenograft Model.* Journal of nuclear medicine : official publication, Society of Nuclear Medicine, 2011. **52**(11): p. 1764-1769.
19.	Boschi, F., et al., *In vivo 18 F-FDG tumour uptake measurements in small animals using Cerenkov radiation.* European Journal of Nuclear Medicine and Molecular Imaging, 2010: p. 1-8.
20.	Park, J.C., et al., *Facile preparation of a hybrid nanoprobe for triple-modality optical/PET/MR imaging.* Small, 2010. **6**(24): p. 2863-8.
21.	Holland, J.P., et al., *Intraoperative Imaging of Positron Emission Tomographic Radiotracers Using Cerenkov Luminescence Emissions.* Moleclar Imaging, 2011. **10**(3): p. 177-186.
22.	Jeong, S.Y., et al., *Combined Cerenkov luminescence and nuclear imaging of radioiodine in the thyroid gland and thyroid cancer cells expressing sodium iodide symporter : Initial feasibility study.* Endocrine Journal, 2011. **Adv. Pub**: p. 1-9.
23.	Spinelli, A.E., et al., *First human Cerenkography.* Journal of Biomedical Optics, 2013. **18(2)**: p. 020502-1 - 020502-3.

24. Thorek, D.L., et al., *Positron lymphography: multimodal, high-resolution, dynamic mapping and resection of lymph nodes after intradermal injection of 18F-FDG.* J Nucl Med, 2012. **53**(9): p. 1438-45.
25. Kothapalli, S.-R., et al., *Endoscopic imaging of Cerenkov luminescence.* Biomedical Optics Express, 2012. **3**(6): p. 1415-1420.
26. Ross, H., *Measurement of β-emitting nuclides using Cerenkov radiation.* Analytical Chemistry, 1969. **41**(10): p. 1260-1265.
27. Li, C., G.S. Mitchell, and S.R. Cherry, *Cerenkov Luminescence Tomography for Small Animal Imaging.* Optics Letters, 2010. **35**(7).
28. Khalil, M.M., *Positron Tomography (PET): Basic Principles*, in *Basic Sciences of Nuclear Medicin*, M.M. Kahalil, Editor. 2011, Springer-Verlag.
29. Cherry, S.R. and M. Dahlbom, *PET: Physics, Instrumentation, and Scanners*. 2006: Springer New York.
30. Roß, T. and S. Ametamey, *PET Chemistry: An Introduction*, in *Basic Sciences of Nuclear Medicine*, M.M. Kahalil, Editor. 2011, Springer-Verlag Berlin Heidelberg.
31. N.E.M.A., *NEMA NU 2-2012 Performance Measurements of Positron Emission Tomographs*, 2012, National Electrical Manufacturers Association.
32. N.E.M.A, *NEMA Standards Publication NU 4 - 2008 Performance Measurements of Small Animal Positron Emission Tomographs* 2008, National Electrical Manufacturers Association.
33. Goertzen, A.L., et al., *NEMA NU 4-2008 Comparison of Preclinical PET Imaging Systems.* The Journal of Nuclear Medicine, 2012. **53**(8).
34. Månsson, J. *NanoPET/CT*. 2011; Available from: http://www.med.lu.se/bioimaging_center/modalities/pet_spect_ct/nanopet_ct.
35. *Inveon No Limits on Discovery*, 2008, Siemens Medical Solutions USA, Inc.
36. Gu, Z., et al., *Design and Initial Performance of PETbox4, a High Sensitivity Preclinical Imaging Tomograph*, in *2011 IEEE Nuclear Science Symposium Conference Record*.
37. Bai, B., et al., *Performance Comparison of GENISYS4 and microPET Preclinical PET Scanners*, in *2012 IEEE Nuclear Science Symposium and Medical Imaging Conference Record* 2012.
38. Hermann, K., et al., *Evaluation of the Genisys4, a Bench-Top Preclinical PET Scanner.* Journal of Nuclear Medicine, 2013. **54**(7): p. 1 - 6.
39. Ohlerth, S., et al., *Assessment of changes in vascularity and blood volume in canine sarcomas and squamous cell carcinomas during fractionated radiation therapy using quantified contrast-enhanced power Doppler ultrasonography: A preliminary study.* The Veterinary Journal, 2009. **186**: p. 58-63.
40. SHIBUYA, K., et al., *Blood Flow Change Quantification in Cervical Cancer before and during Radiation Therapy Using Perfusion CT.* J. Radiat. Res, 2011. **52**: p. 804–811.
41. Fujii, H., et al., *Tissue oxygenation in a murine SCC VII tumor after X-ray irradiation as determined by EPR spectroscopy.* Radiotherapy and Oncology, 2008. **86**: p. 354–360.
42. Vishwanath, K.e.a., *Quantitative optical spectroscopy can identify long-term local tumor control in irradiated murine head and neck xenografts.* Journal of Biomedical Optics 2009. **14**: p. 54051.